Thin films in hydrodynamic lubrication regime: The Osiris friction setup

Cedric Barazzutti, Juliette Cayer-Barrioz, Denis Mazuyer

▶ **To cite this version:**

Cedric Barazzutti, Juliette Cayer-Barrioz, Denis Mazuyer. Thin films in hydrodynamic lubrication regime: The Osiris friction setup. Review of Scientific Instruments, 2023, 94, pp.065103. 10.1063/5.0155813 . hal-04138268

HAL Id: hal-04138268
https://hal.science/hal-04138268

Submitted on 22 Jun 2023

HAL is a multi-disciplinary open access archive for the deposit and dissemination of scientific research documents, whether they are published or not. The documents may come from teaching and research institutions in France or abroad, or from public or private research centers.

L'archive ouverte pluridisciplinaire **HAL**, est destinée au dépôt et à la diffusion de documents scientifiques de niveau recherche, publiés ou non, émanant des établissements d'enseignement et de recherche français ou étrangers, des laboratoires publics ou privés.

Distributed under a Creative Commons Attribution 4.0 International License

ACCEPTED MANUSCRIPT
Review of Scientific Instruments
AIP Publishing
This is the author's peer reviewed, accepted manuscript. However, the online version of record will be different from this version once it has been copyedited and typeset.
PLEASE CITE THIS ARTICLE AS DOI: 10.1063/5.0151813

Thin Films in Hydrodynamic Lubrication Regime: the Osiris Friction Set-up

Cedric Barazzutti,[1] Juliette Cayer-Barrioz,[1,*] and Denis Mazuyer[1]

[1] *Laboratoire de Tribologie et Dynamique des Systèmes, CNRS UMR 5513, École Centrale de Lyon, 36 avenue Guy de Collongue, 69134 Ecully Cedex, France*

(Dated: May 26, 2023)

A model hydrodynamic lubrication tribometer consisting of two hydrodynamic journal bearings working in thin film conditions was developed in order to investigate the mechanisms of hydrodynamic friction with low-viscosity fluids and the role of surface effects. A small nominal radial clearance of about 5 μm was considered between the two surfaces. This fully instrumented set-up provides in situ information of the sheared fluid film in terms of simultaneous measurements of film thickness, localization and extension of the cavitation zone with a resolution of 30°, nominal friction torque up to 0.5 $N.m$ with an accuracy of 0.05 $mN.m$, temperature and position of the shaft for velocities up to 12000 rpm. To illustrate the capability of the Osiris tribometer, thin hydrodynamic film measurements were performed for smooth surfaces. The results are presented here and thermal effects, acceleration and inertia contributions were discussed. Finally, the influence of the surface topography using textured surfaces was demonstrated and the role of adsorbed layers on the surface due to fluid formulation was highlighted.

1. INTRODUCTION

In hydrodynamic lubrication regime, the surfaces are fully separated by a fluid film that carries the applied load. A pressure field is therefore generated to ensure a constant flow rate of the fluid within the contact. In this lubrication regime, surfaces are not deformed as pressures remain relatively moderate, of the order of magnitude of few 100 kPa. Hydrodynamic friction is relatively low and mainly results from the viscous properties of the sheared fluid and from the entrainment velocity. This regime is particularly of concern in many engineering applications, such as thrusts and journal bearings of various geometries [1][2][3].

A journal bearing is typically composed of a shaft and a housing animated by a relative motion and separated by a fluid film. Due to loading from the weight of the shaft itself combined with a possible additional mass and/or due to misalignment, the shaft is never centred in the bearing, leading to a film distribution. This eccentricity induces a variation of pressure and creates a convergent zone in the contact inlet, where the film is thicker. The hydrodynamic pressure within the fluid generated in this area increases the load capacity of the bearing, which is responsible for the surface separation. At the contact outlet, in the divergent area, the pressure rapidly diminishes, resulting in a fluid film rupture, commonly referred to as cavitation zone [4][5][6].

The fluid flow obeys Reynolds equation in the framework of thin film lubrication assumptions. Numerous numerical simulations (see for instance [2][6][7][8][9][10]) have been developed in the literature to predict the film thickness distribution as well as the pressure field and to describe the dynamic stability of the journal bearings.

*The author to whom correspondence may be addressed: juliette.cayer-barrioz@ec-lyon.fr

Nevertheless, as fluid viscosity decreases more and more to lower viscous dissipation and as geometrical constraints lead to smaller gap, the film thickness decreases down to few micrometers and surface effects including surface texturing and/or thin adsorbed layers play a key role in the friction evolution and in the film formation mechanisms. These surface effects are less likely accounted for by numerical models or by experimental instrumented test rigs with thick hydrodynamic films [7][11][12].

The goal of this paper is to describe the model hydrodynamic lubrication tribometer that was developed in order to investigate the lubrication mechanisms in thin hydrodynamic fluid films. This fully instrumented set-up allows one to get in situ access to the sheared fluid film in terms of simultaneous measurements of film thickness, friction torque, temperature and position of the shaft. The apparatus is described in detail and the measurements and the associated in situ analysis are presented and discussed. An illustration of the surface effect is also given with tests performed for a textured surface and for a formulated oil.

2. THE OSIRIS FRICTION SET-UP

This apparatus, designed in the Laboratoire de Tribologie et Dynamique des Systemes (LTDS) at Ecole centrale de Lyon, is composed of two journal bearings working in oil bath, with a nominal radial clearance of 5 μm (see Figure 1). A dedicated in situ instrumentation allows one to simultaneously measure the fluid film thickness and the friction torque, the position of the shaft and the temperature of the fluid for controlled velocities up to 12000 rpm, that is to say 6.3 $m.s^{-1}$, and controlled accelerations until 16 $m.s^{-2}$ [9] [13].

This apparatus was designed to easily and rapidly investigate the hydrodynamic lubrication mechanisms for thin films, the role of both the fluid rheology and

ACCEPTED MANUSCRIPT
Review of Scientific Instruments
AIP Publishing
This is the author's peer reviewed, accepted manuscript. However, the online version of record will be different from this version once it has been copyedited and typeset.
PLEASE CITE THIS ARTICLE AS DOI: 10.1063/5.0155583

chemistry, the impact of textured surfaces as well as the influence of loading.

2.1. Tribometer description and journal bearing geometry

The tribometer consists in an aluminium plate of dimensions 0.2 x 0.4 m^2 on which is located a brushless servomotor (Parker NV3010EAW) reaching a rotating velocity of 12 000 rpm with a nominal torque of 1.8 $N.m$. This motor drives in rotation a shaft of length 182 mm and of diameter, D, equal to 10 mm. This shaft rotates within two stationary bearings of axial length, L, of 16 mm with an order of magnitude of the nominal radial clearance of 5 μm. The bearing ratio L/D is 1.6 [13].

Two oil columns, each containing few $100mL$, feed the bearings by gravity. The temperature of the oil reservoir, close to the bearing area of interest (see inset Figure 1), is measured using four temperature probes (K-type thermocouple, TC Direct). They were placed on each side of the bearing due to the limited space within the bearing.

The friction torque is measured for the two bearings via a torquemeter Magtrol TM303 up to 0.5 $N.m$ with a resolution of 5.10^{-4} $N.m$, located between the motor and the first journal bearing.

To ensure the oil supply of the bearings without additional friction, *viscoseal* dynamic sealing with helicodal grooves was used on each side of the bearing.

The description of the Osiris tribometer is presented in Figure 1.

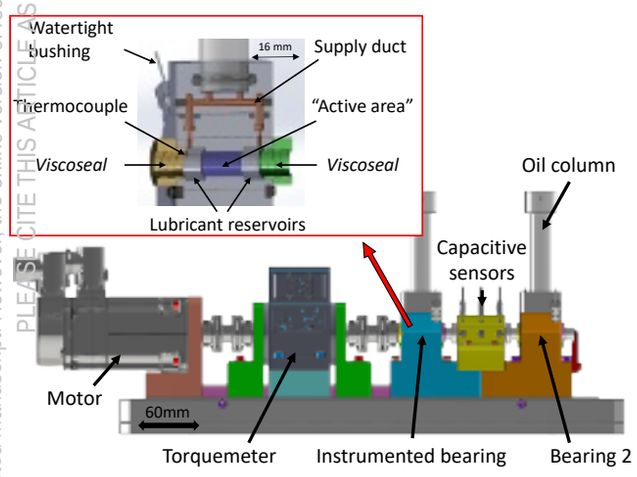

Figure 1: *Schematic of the Osiris tribometer. The inset shows a zoom of the bearing. The various sensors of the tribometer are also indicated.*

2.2. Film thickness measurement

2.2.1. Shaft position

To follow the position of the shaft during an experiment, six capacitive sensors from Fogale were located along the shaft. Due to space restrictions, these sensors were positioned between the two bearings. They were organized by pairs, at 90° from each other, perpendicular to the shaft axis and in three separate measurement planes [9]. The measurement range is 0-300 μm with a resolution of 3.10^{-3} μm. The acquired signal is a voltage 0-10 V proportional to the distance at a maximum frequency of $10kHz$.

2.2.2. Film thickness and cavitation zone

In order to access the film thickness distribution within the bearing, one bearing was instrumented with 12 ultrasonic sensors provided by Tribosonics Ltd. distributed uniformly along its circumference as shown in Figure 2. These sensors consist in piezoelectric elements working as transmitter and receiver of ultrasonic waves at a frequency of $1kHz$. Based on the interface stiffness methodology [14][15], they allow one to measure oil film thickness ranging from 0.1 to 50 μm (provided the appropriate calibration) and its distribution as well as to detect the existence of the cavitation zone.

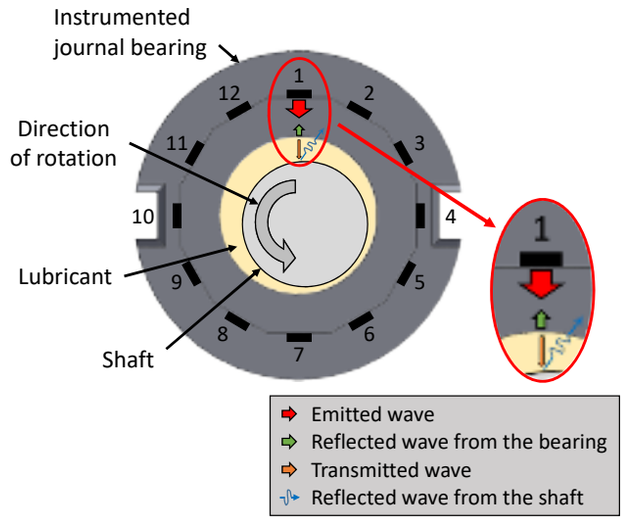

Figure 2: *Schematic of the ultrasonic sensors distributed along the bearing*

ACCEPTED MANUSCRIPT
Review of Scientific Instruments
AIP Publishing
This is the author's peer reviewed, accepted manuscript. However, the online version of record will be different from this version once it has been copyedited and typeset.
PLEASE CITE THIS ARTICLE AS DOI: 10.1063/1.5055813

2.3. Monitoring and acquisition

Commercial software such as Torque7 and xSCAN Configurator were used to acquire torquemeter and ultrasonic sensors signals. In addition, a LabVIEW software was developed to control the motor and acquire data from the motor, the thermocouples and the capacitive sensors. All data were acquired with four channel cards from National Instruments NI 9239 and NI9210. A synchronization of all the signals was performed at the onset of rotation of the shaft.

3. MEASUREMENT AND RESULTS

In the following part, typical experimental results and the tribometer validation are presented. They were obtained for a group III+ base oil of low viscosity, $\eta = 26.8 mPa.s$ at $25°C$ and a smooth shaft. The radial clearance was 5.38 μm. The experimental protocol consisted in a ramp of acceleration until a target rotating velocity, which is kept constant for around $1h30$, and finally a ramp of deceleration. All the experiments were performed at least twice.

3.1. Frictional and thermal response of a sheared fluid film

Illustrative experiments were carried out at an acceleration of 0.063 $m.s^{-2}$ until the target velocity of 1.57 $m.s^{-1}$ (3000 rpm) that was maintained constant for $1h30$ before decelerating at 0.063 $m.s^{-2}$. Figure 3.a presents the evolution of the measured torque and oil column temperature as a function of the time for this controlled kinematics. At the onset of the shaft rotation, a peak of torque was detected as shown in Figure 3.b. The value of this peak results from the movement of the shaft, lifted away from the bearing surface. During the acceleration phase, the torque increases with the velocity. A maximum torque is measured once the target velocity is reached, before a decrease in torque during the constant velocity step until a steady-state torque value. The simultaneous variation of the oil column temperature shows that the temperature is quasi constant, $+0.2°C$, during this acceleration phase. It increases then dramatically of $7°C$ during the constant velocity step.

3.2. Validation of the tribometer

In order to validate the tribometer and especially the torque values, experiments were performed for a step of constant velocity. The value of the constant velocity varied up to 3.67 $m.s^{-1}$ (7000 rpm). The values of the maximum torque, measured at the end of the deceleration phase and of the steady-state torque, measured at the end of the constant velocity step, were plotted vs the velocity - see Figure 4.a and .b.

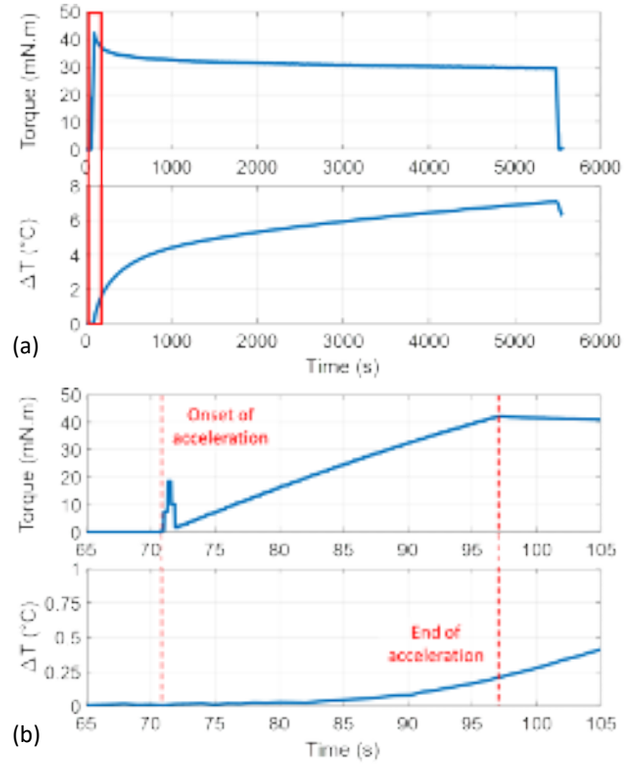

Figure 3: *Typical evolution of the torque and of the variation of temperature in the oil reservoir as a function of the velocity for an acceleration of 0.063 $m.s^{-2}$ followed by a velocity plateau at 1.57 $m.s^{-1}$ before a deceleration, for a base oil of initial viscosity $\eta = 26.8$ mPa.s at $25°C$ and a smooth shaft (a) and zoom on the acceleration phase (b).*

In a first qualitative approach to validate the hydrodynamic friction set-up, one can consider that, for a centred shaft in the bearing, neglecting the existence of cavitation, the viscous flow follows a Couette flow. It is then possible to calculate the shear stress and the torque as a function of the viscosity. The shear stress is:

$$\tau = \frac{\eta.U}{C_r} \tag{1}$$

with U the shaft velocity and C_r the radial clearance.

The torque in one bearing can then be calculated as follows:

$$C = \frac{2\pi.\eta.U.D^2.L}{4.C_r} \tag{2}$$

During the acceleration phase, the torque measured for two bearings increases linearly with the velocity as predicted by equation 2.

ACCEPTED MANUSCRIPT
Review of Scientific Instruments
AIP Publishing
This is the author's peer reviewed, accepted manuscript. However, the online version of record will be different from this version once it has been copyedited and typeset.
PLEASE CITE THIS ARTICLE AS DOI: 10.1063/1.5055813

The theoretical maximum torque was calculated by assuming an athermal process during the acceleration phase and therefore a fluid viscosity equal to the one at $25°C$. These values of torque were compared to the measured experimental ones in Figure 4.a. The values remain of the right order of magnitude. The agreement between the two values is perfect below a velocity of 1.57 $m.s^{-1}$. Above this velocity, the theoretical values diverge from the measured ones. One can assume that thermal effects, neglected at first, generated during the slow increase in velocity at an acceleration of 0.063 $m.s^{-2}$, can explain the decrease in viscosity and the diminution of the measured viscous torque.

In the case of the steady-state torque value, the increase in temperature in the reservoir and the associated decrease in viscosity, were taken into account during each constant velocity step, assuming that the variation of temperature in the reservoir was representative of that in the bearing. The evolution of the theoretical and measured steady-state torques follows the same trend with the increase in velocity (see Figure 4.b). Once again, the calculated values are larger than the measured ones, despite being of the same order of magnitude. This could be explained by a small difference in temperature between the reservoir and the bearing and/or the non-centred shaft and/or the existence of a cavitation zone.

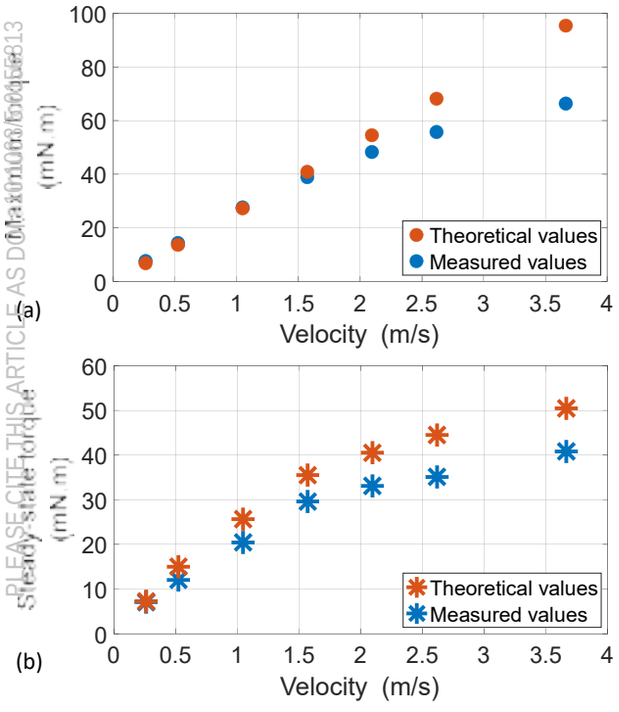

Figure 4: *Comparative evolution of the maximum torque (a) and of the steady-state torque (b) versus velocity between measured and theoretical values, assuming a Couette flow without cavitation.*

3.3. Role of the velocity: thermal effects

To highlight the thermal effects on the friction response of the fluid film, the velocity was varied. Experiments were performed with the same acceleration value until a target velocity of either 1.57 or 3.67 $m.s^{-1}$, that was maintained for a step of $1h30$. Figure 5 shows the evolution of the torque and of the temperature variation with time. The torque evolution remains similar. During the acceleration phase, the torque values superimpose perfectly. During the constant velocity step, the torque values are superior at higher velocity, in agreement with equation 2. It can be seen that the torque strongly decreased in the first $10minutes$ of the experiment as 70% of the final value was attained. However, the variation of temperature differs as a function of the time during this velocity plateau: the variation of temperature reached $18°C$ at the highest velocity, compared to $7°C$ at 1.57 $m.s^{-1}$. Although the temperature is not stabilized at the end of the steady-state regime velocity, it can be seen that the temperature strongly increased in the first $10minutes$ of the experiment as 60-70% of the final value was attained. This evolution is also in agreement with the stabilization of the torque values. We confirm here that shearing the thin fluid film at higher velocity increases the thermal dissipation as expected.

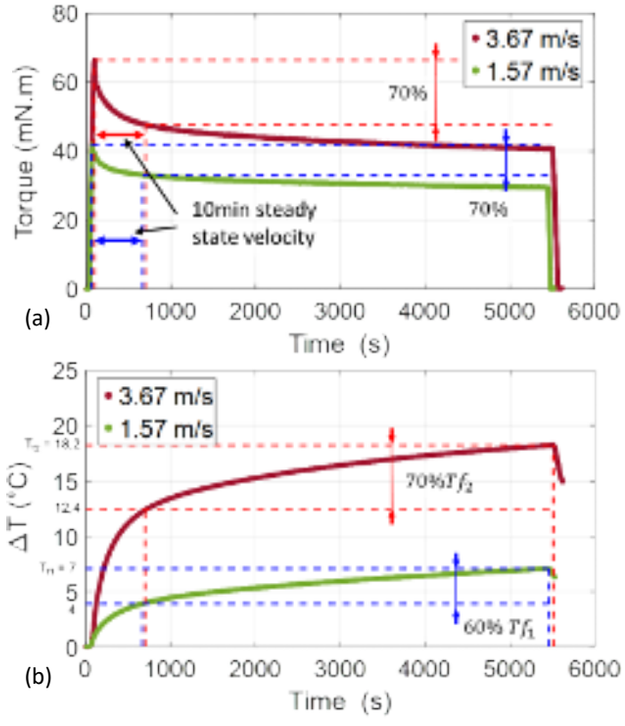

Figure 5: *Influence of the velocity on the evolution of the torque (a) and of the variation of temperature in the oil column (b) versus time.*

In the following parts, this time duration of 10 *minutes*

and the target velocity of 3.67 $m.s^{-1}$ (7000 rpm) was chosen.

3.4. Role of the acceleration: thermal and inertia contribution

In this paragraph, only the effect of the acceleration phase was investigated on the temperature variation evolution and the torque. The acceleration was varied from 0.031 to 15.7 $m.s^{-2}$ up to a velocity of 3.67 $m.s^{-1}$. Depending on the acceleration, the variation of temperature could reach 3.4°C at the slowest acceleration as shown in Figure 6, indicating that the acceleration phase is only purely athermal for acceleration above 1.57 $m.s^{-2}$.

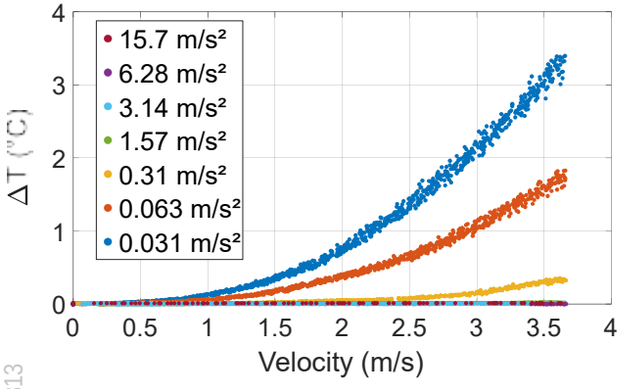

Figure 6: *Influence of the acceleration on the evolution of the variation of temperature in the oil column up to a velocity of 3.67 $m.s^{-1}$.*

The corresponding torque evolution clearly indicates a strong dependence with the acceleration (see Figure 7): the torque values were shifted to higher values as the acceleration increases.

This was the signature of the inertia contribution of the mechanical parts at the onset of rotation. The inertia contribution was also visible during the experiment at the end of acceleration and at the onset of deceleration: a sudden drop of the torque was detected. The values of the drop were similar at these two instants, depending mainly on the acceleration/deceleration value. In order to fully characterize the inertia contribution, the values of the inertial torque measured experimentally (averaged on the two values measured at each drop for each experiment) were compared to the calculated value, as a function of the acceleration, and reported in table I. The theoretical values were calculated with:

$$C_i = \frac{\omega.I}{\delta t} \tag{3}$$

where C_i is the inertial torque, I is the inertia of the system taking into account the rotating mechanical elements equal to 553 $g.cm^2$, ω the angular velocity and δt the duration of the acceleration phase.

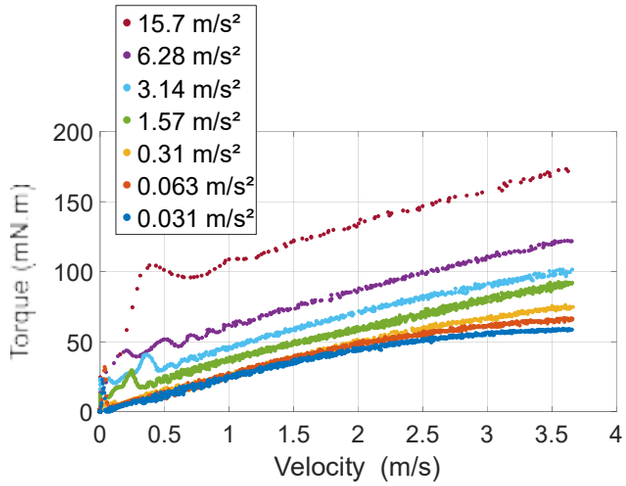

Figure 7: *Influence of the acceleration on the evolution of the torque up to a velocity of 3.67 $m.s^{-1}$.*

Acceleration ($m.s^{-2}$)	Measured inertial torque C_i ($mN.m$)	Calculated inertial torque C_i ($mN.m$)
0.031	0.19 ± 0.02	0.18
0.063	0.23 ± 0.03	0.35
0.31	1.6 ± 0.1	1.7
1.57	8.4 ± 0.9	8.9
3.14	16.4 ± 1.7	17.9
6.28	34.4 ± 3.5	35.8
15.7	80.1 ± 8.0	89.6

Table I: *Comparison between the measured and calculated inertial torque C_i as a function of the acceleration*

A good agreement was obtained between the calculated values and the ones measured experimentally. The small discrepancy was attributed to geometrical errors. This analysis confirms that the drop in torque, observed experimentally, resulted from the inertia.

3.5. In situ analysis of the film forming mechanisms

3.5.1. Eccentricity analysis

Using the six capacitive sensors gives access to the position of the shaft compared to the bearing, in each measurement plane. Knowing the relative distance from the sensor to the shaft surface, in two points M and N, the position of the center $O(a, b)$ of the shaft is given by:

ACCEPTED MANUSCRIPT
Review of Scientific Instruments
AIP Publishing
This is the author's peer reviewed, accepted manuscript. However, the online version of record will be different from this version once it has been copyedited and typeset.
PLEASE CITE THIS ARTICLE AS DOI: 10.1063/1.5155813

ACCEPTED MANUSCRIPT
Review of Scientific Instruments
AIP Publishing
This is the author's peer reviewed, accepted manuscript. However, the online version of record will be different from this version once it has been copyedited and typeset.
PLEASE CITE THIS ARTICLE AS DOI: 10.1063/5.0155...

$$a = \frac{X_M}{2} - \frac{Z_N}{2}.\sqrt{\frac{D^2 - {X_M}^2 - {Z_N}^2}{{X_M}^2 + {Z_N}^2}} \quad (4)$$

$$b = \frac{Z_N}{2} - \frac{X_M}{2}.\sqrt{\frac{D^2 - {X_M}^2 - {Z_N}^2}{{X_M}^2 + {Z_N}^2}} \quad (5)$$

This allows one to calculate and plot the orbits of movement of the shaft center. The orbits present a specific shape related to each couple shaft-bearing due to geometrical defects as well as possible misalignment. These measurement artefacts can be eliminated by an adequate frequency filtering. A bandpass filter was used to isolate the main frequency, representative of the shaft rotation. These orbits exhibit different amplitudes in each measurement plane, indicating that the shaft was deformed during the rotation (see Figure 8.a).

Assuming a polynomial extrapolation of second order as proposed in [9], it is then possible to determine the position of the shaft center, along the shaft length, and therefore in the bearings. Figure 8 presents the extrapolated 3D orbit of the shaft. The amplitude varies in each bearing, due to the presence of a mechanical coupling with the motor and the torquemeter: this limits the movement amplitude in the first bearing (see inset c) compared to the second one. This strong initial assumption offers the advantage of an easily-obtained qualitative information regarding the shaft position.

This analysis provides the evolution of the shaft position as a function of time during the experiment. The film thickness, h, can then be calculated:

$$h = C_r.(1 + \epsilon.cos\theta) \quad (6)$$

with ϵ the relative eccentricity and θ a given angle. Figure 9 presents the evolution of the mean and maximal eccentricity and of the corresponding minimum film thickness in the mid-plane of bearing 1. At first, the eccentricity decreases, indicating the lift of the shaft. Once the constant velocity step reached, the eccentricity decreases again, representing the centering of the orbits in the bearings, before stabilization. It remains constant for the rest of the steady-state regime. The film thickness evolution is directly correlated to the eccentricity evolution.

This first rough analysis does not account for the existence of cavitation.

3.5.2. *Film thickness distribution and cavitation zone localization*

In order to better estimate the film thickness distribution, ultrasonic sensors were used. Nevertheless, an accurate measurement of the film thickness itself, based on

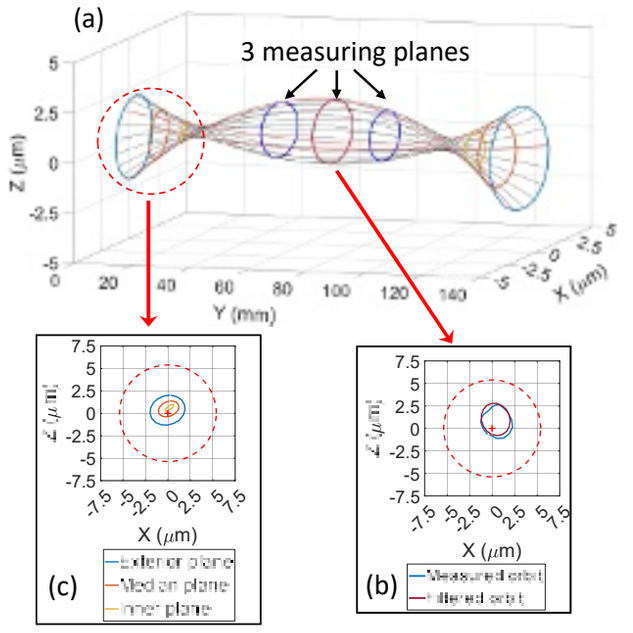

Figure 8: *(a) 3D orbit extrapolated from the positions of the shaft center at the end of the steady-state regime. The three measurement planes are represented as well as the instrumented bearing on left and the bearing 2 on the right. The inset (b) represents the measurement before and after filtering in the second measurement plane. The inset (c) shows the extrapolated orbits of the shaft center in the instrumented bearing.*

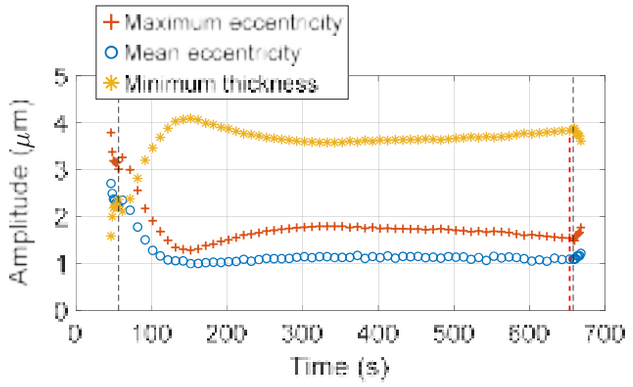

Figure 9: *Time evolution of the mean and maximum eccentricity as well as the minimum film thickness, calculated within the instrumented bearing.*

the interface stiffness methodology developed by [14][15], requires a calibration with neither the shaft, nor the oil to define the reference in film thickness. In addition, the evolution of the wave propagation velocity in the fluid (for each fluid) as a function of the temperature as well as the acoustic impedance of the solids need to be known. In this context, the ultrasonic sensors were here only used

ACCEPTED MANUSCRIPT
Review of Scientific Instruments
AIP Publishing
This is the author's peer reviewed, accepted manuscript. However, the online version of record will be different from this version once it has been copyedited and typeset
PLEASE CITE THIS ARTICLE AS DOI: 10.1063/5.0153883

to detect the presence of cavitation in the bearing and to determine its extension.

The estimate of the cavitation zone position and extension can be performed with a accuracy of 30° as a result of the geometrical distribution of the twelve sensors along the bearing circumference. During the steady-state regime, at constant velocity, the orbits can be considered as stable and constant. A relative variation of the mean film thickness can be qualitatively detected and translated in three different relative levels of thickness defined as $+$, $+-$ and $-$. Each sensor providing one level, the distribution of the film thickness can be extrapolated along the circumference of the bearing. Knowing the direction of rotation and considering the position of the shaft where the maximum of the eccentricity is achieved, the cavitation zone can then be estimated and localized, in the contact divergent (see Figure 10 for instance, corresponding at a time of 572 s in steady-state regime at a constant velocity of 3.67 $m.s^{-1}$.

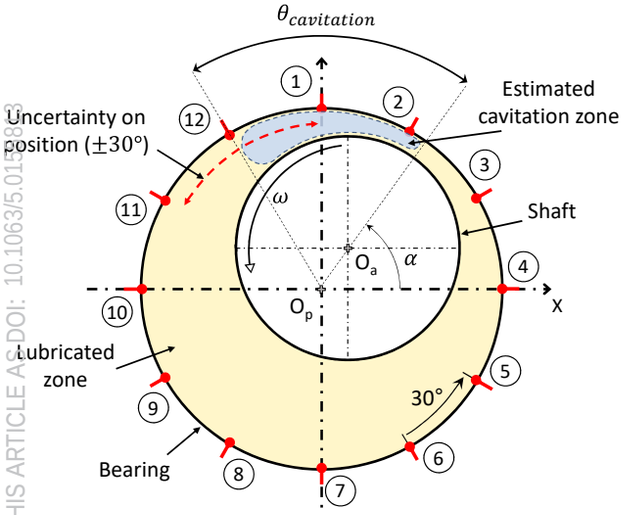

Figure 10: *Example of localization of the cavitation zone and estimate of its extension at the end of the steady-state regime in the instrumented bearing.*

This analysis provides an approximate evolution of the cavitation zone extension as a function of the time as shown in Figure 11 in the first bearing. The extension of the cavitation zone seems to increase at first, before decreasing and reaching a stable value after 300 s. From the instantaneous estimate of the shaft position and the cavitation length, the inlet zone can be deduced.

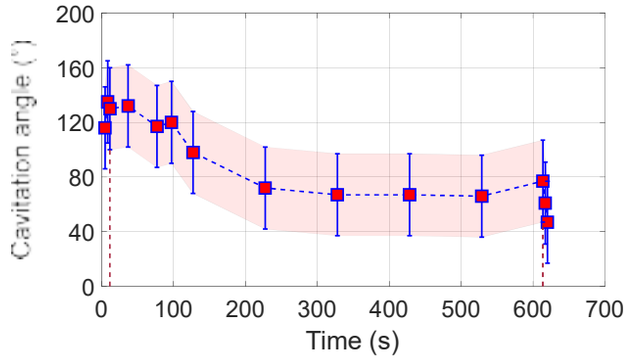

Figure 11: *Cavitation length estimated as a function of time in the instrumented bearing.*

4. CAPABILITY TO DETECT SURFACE EFFECTS

4.1. Influence of the surface texturing on the friction and cavitation extension

In order to demonstrate the capability of the Osiris tribometer, experiments with femtosecond LASER-textured surfaces with a cavity density of about 15% and cavity 2 μm deep were performed at a target velocity of 3.67 $m.s^{-1}$ and an acceleration of 0.31 $m.s^{-2}$. An increase of 8% in friction torque was detected compared to the one measured for the smooth surface, associated with a diminution of the cavitation length extension as shown in Figure 12. The maximum eccentricity ratio increased at 0.4 for the considered textured surface while it was about 0.2 for the smooth surface.

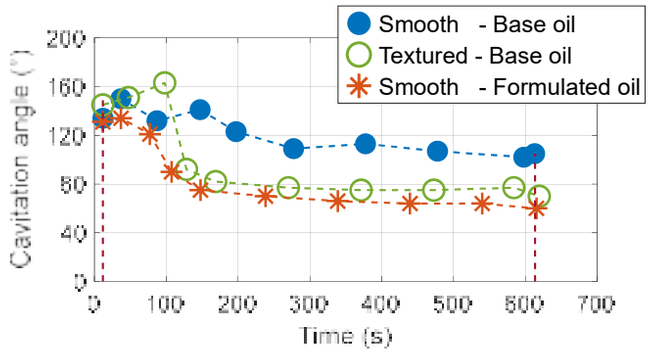

Figure 12: *Cavitation length estimated as a function of time in the instrumented bearing for a textured surface compared to the smooth one for a base oil and for a formulated oil with a smooth surface.*

ACCEPTED MANUSCRIPT
Review of Scientific Instruments
AIP Publishing
This is the author's peer reviewed, accepted manuscript. However, the online version of record will be different from this version once it has been copyedited and typeset.
PLEASE CITE THIS ARTICLE AS DOI: 10.1063/5.0153...

4.2. Influence of the oil formulation

Formulated oils of viscosity around $40mPa.s$ were also tested on smooth surfaces. The extension of the cavitation length was impacted by the presence of the poly(alkyl)metacrylate additives known to adsorb on the surfaces to form boundary layers [16]: a decrease in the cavitation length of 30° was measured compared to those measured with base oil (see Figure 12). In parallel, the friction torque slightly increased. These results confirmed the capability of the Osiris tribometer to detect surface effects even in hydrodynamic lubrication regime.

5. SUMMARY

This Osiris model tribometer working in thin film conditions and hydrodynamic lubrication regime combines simultaneous friction and in situ measurements of shaft position, film thickness distribution, localization and extension of the cavitation zone and temperature for a controlled contact kinematics. The nominal radial clearance was about 5 μm. The validation of the tribometer was perfomed by confronting the measured friction torque values up to 0.5 $N.m$ to calculated ones, using a simplified framework of assumptions.

By changing the velocity up to 4 $m.s^{-1}$ and the controlled acceleration up to 16 $m.s^{-2}$ $m.s^{-2}$, we were able to discriminate and discuss the thermal and the inertial relative contributions. The latter was further validated by a comparison with theoretical values of inertial torque. To further analyze the in situ mechanisms within the bearing, capacitive sensors and their associated geometrical analysis provided the extrapolated position of the shaft and allowed one to deduce the eccentricity. The minimum film thickness was therefore calculated in the bearing. The film thickness distribution was analyzed and the cavitation localization and extension were estimated with a resolution of 30°.

Finally, the Osiris ability to detect low friction and small variation of friction induced by surface effects was demonstrated by performing tests with textured surfaces. We illustrated in this example that the length of the cavitation zone was reduced resulting in an increase in friction torque. We also highlighted the role of the fluid formulation with the existence of an adsorbed boundary layer on the surface that modified the extension of the cavitation zone.

This apparatus showed its capability to detect small variation in friction correlated with film thickness distribution and shaft position, opening innovative research path for coating and texturing development as well as low viscosity fluid formulation such as environmentally-friendly aqueous lubricants. An advantage of this tribometer is the need of small volumes of fluid. In addition, the in situ measurements provide input data for numerical simulations in order to improve the understanding of the hydrodynamic lubrication mechanisms, especially in thin film conditions and with textured surfaces.

Acknowledgments

This research was financially supported by the ADEME, the French Agency for the ecological transition, via the IMOTEP project.

[1] J. Frene *Butes et Paliers Hydrodynamiques* (Techniques de l'Ingenieur, 1995)
[2] G. W. Stachowiak and A. W. Batchelor *Engineering Tribology* (Elsevier, 3rd edition, 2005)
[3] M. M. Khonsari and E. R. Booser *Applied Tribology: Bearing Design and Lubrication* (Wiley, 3rd edition, 2017)
[4] P. D. Swales *A Review of Cavitation Phenomena in Engineering Situations* (In C. M. Taylor et al editors, Proceedings of the 1st Leeds-Lyon Symposium in Tribology, 3-9, 1974)
[5] D. Dowson and C. M. Taylor *Cavitation in Bearings* (Annual Review of Fluid Mechanics, 1979)
[6] M. J. Braun and W. H. Hannon *Cavitation Formation and Modelling for Fluid Film Bearings: A Review* (Journal of Engineering Tribology, 224: 839-863, 2010)
[7] R. Boncompain, M. Fillon and J. Frene *Analysis of Thermal Effects in Hydrodynamic Bearings* (ASME Journal of Tribology, 108(2): 219-224, 1986)
[8] T. Woloszynski, P. Podsiado and G. W. Stachowiak *Efficient Solution to the Cavitation Problem in Hydrodynamic Lubrication* (Tribology Letters, 58: 1-11, 2015)
[9] J. Rebufa *Vibrations de ligne d'arbre sur paliers hydrodynamiques: influence de l'etat de surface* (PhD thesis, 2016-LYSEC44, Ecole centrale de Lyon, 2016)
[10] J. Rebufa, F. Thouverez, E. Le Guyadec and D. Mazuyer *Nonlinear Effects of Surface Texturing on the Performance of Journal Bearings in Flexible Rotordynamic Systems* (ASME. Journal of Tribology, 139(5): 051705, 2017).
[11] C. Giraudeau *Influence des discontinuits gomtriques sur les performances des paliers en rgime thermolastohydrodynamique (TEHD)* (PhD thesis, Universite de Poitiers, 2016)
[12] B. Pap *Modelisation d'un palier hydrodynamique de reducteur epicyclodal oprant en conditions severes* (PhD thesis, Universite de Poitiers, 2018)
[13] C. Barazzutti *Effets de surface sur le comportement tribologique d'un palier hydrodynamique* (PhD thesis, 2023ECDL0002, Ecole centrale de Lyon, 2023)
[14] R. S. Dwyer-Joyce, P. Harper and B. W. Drinkwater *A Method for the Measurement of Hydrodynamic Oil Films using Ultrasonic Reflection* (Tribology Letters, 17(2): 337-348, 2004)
[15] S. Kasplang and R. S. Dwyer-Joyce *Observations of Film Thickness Profile and Cavitation around a Journal Bear-*

ing Circumference (Tribology Transactions, 51(2): 231-245, 2008)

[16] F. Abouhadid *Aspects moleculaires du frottement limite: couplage entre structure des additifs et physico-chimie des surfaces* (PhD thesis, 2021-LYSEC48, Ecole centrale de Lyon, 2021)

AIP Publishing

Review of Scientific Instruments

ACCEPTED MANUSCRIPT

This is the author's peer reviewed, accepted manuscript. However, the online version of record will be different from this version once it has been copyedited and typeset.

PLEASE CITE THIS ARTICLE AS DOI: 10.1063/5.0155813

ACCEPTED MANUSCRIPT
Review of Scientific Instruments
AIP Publishing
This is the author's peer reviewed, accepted manuscript. However, the online version of record will be different from this version once it has been copyedited and typeset.
PLEASE CITE THIS ARTICLE AS DOI: 10.1063/5.0155813

Thin Films in Hydrodynamic Lubrication Regime: the Osiris Friction Set-up

Cedric Barazzutti,[1] Juliette Cayer-Barrioz,[1,*] and Denis Mazuyer[1]

[1] *Laboratoire de Tribologie et Dynamique des Systèmes, CNRS UMR 5513, École Centrale de Lyon, 36 avenue Guy de Collongue, 69134 Ecully Cedex, France*

(Dated: May 26, 2023)

A model hydrodynamic lubrication tribometer consisting of two hydrodynamic journal bearings working in thin film conditions was developed in order to investigate the mechanisms of hydrodynamic friction with low-viscosity fluids and the role of surface effects. A small nominal radial clearance of about 5 μm was considered between the two surfaces. This fully instrumented set-up provides in situ information of the sheared fluid film in terms of simultaneous measurements of film thickness, localization and extension of the cavitation zone with a resolution of 30°, nominal friction torque up to 0.5 $N.m$ with an accuracy of 0.05 $mN.m$, temperature and position of the shaft for velocities up to 12000 rpm. To illustrate the capability of the Osiris tribometer, thin hydrodynamic film measurements were performed for smooth surfaces. The results are presented here and thermal effects, acceleration and inertia contributions were discussed. Finally, the influence of the surface topography using textured surfaces was demonstrated and the role of adsorbed layers on the surface due to fluid formulation was highlighted.

1. INTRODUCTION

In hydrodynamic lubrication regime, the surfaces are fully separated by a fluid film that carries the applied load. A pressure field is therefore generated to ensure a constant flow rate of the fluid within the contact. In this lubrication regime, surfaces are not deformed as pressures remain relatively moderate, of the order of magnitude of few 100 kPa. Hydrodynamic friction is relatively low and mainly results from the viscous properties of the sheared fluid and from the entrainment velocity. This regime is particularly of concern in many engineering applications, such as thrusts and journal bearings of various geometries [1][2][3].

A journal bearing is typically composed of a shaft and a housing animated by a relative motion and separated by a fluid film. Due to loading from the weight of the shaft itself combined with a possible additional mass and/or due to misalignment, the shaft is never centred in the bearing, leading to a film distribution. This eccentricity induces a variation of pressure and creates a convergent zone in the contact inlet, where the film is thicker. The hydrodynamic pressure within the fluid generated in this area increases the load capacity of the bearing, which is responsible for the surface separation. At the contact outlet, in the divergent area, the pressure rapidly diminishes, resulting in a fluid film rupture, commonly referred to as cavitation zone [4][5][6].

The fluid flow obeys Reynolds equation in the framework of thin film lubrication assumptions. Numerous numerical simulations (see for instance [2][6][7][8][9][10]) have been developed in the literature to predict the film thickness distribution as well as the pressure field and to describe the dynamic stability of the journal bearings.

*The author to whom correspondence may be addressed: juliette.cayer-barrioz@ec-lyon.fr

Nevertheless, as fluid viscosity decreases more and more to lower viscous dissipation and as geometrical constraints lead to smaller gap, the film thickness decreases down to few micrometers and surface effects including surface texturing and/or thin adsorbed layers play a key role in the friction evolution and in the film formation mechanisms. These surface effects are less likely accounted for by numerical models or by experimental instrumented test rigs with thick hydrodynamic films [7][11][12].

The goal of this paper is to describe the model hydrodynamic lubrication tribometer that was developed in order to investigate the lubrication mechanisms in thin hydrodynamic fluid films. This fully instrumented set-up allows one to get in situ access to the sheared fluid film in terms of simultaneous measurements of film thickness, friction torque, temperature and position of the shaft. The apparatus is described in detail and the measurements and the associated in situ analysis are presented and discussed. An illustration of the surface effect is also given with tests performed for a textured surface and for a formulated oil.

2. THE OSIRIS FRICTION SET-UP

This apparatus, designed in the Laboratoire de Tribologie et Dynamique des Systemes (LTDS) at Ecole centrale de Lyon, is composed of two journal bearings working in oil bath, with a nominal radial clearance of 5 μm (see Figure 1). A dedicated in situ instrumentation allows one to simultaneously measure the fluid film thickness and the friction torque, the position of the shaft and the temperature of the fluid for controlled velocities up to 12000 rpm, that is to say 6.3 $m.s^{-1}$, and controlled accelerations until 16 $m.s^{-2}$ [9] [13].

This apparatus was designed to easily and rapidly investigate the hydrodynamic lubrication mechanisms for thin films, the role of both the fluid rheology and

ACCEPTED MANUSCRIPT
Review of Scientific Instruments
AIP Publishing
This is the author's peer reviewed, accepted manuscript. However, the online version of record will be different from this version once it has been copyedited and typeset.
PLEASE CITE THIS ARTICLE AS DOI: 10.1063/5.0155813

chemistry, the impact of textured surfaces as well as the influence of loading.

2.1. Tribometer description and journal bearing geometry

The tribometer consists in an aluminium plate of dimensions 0.2 x 0.4 m^2 on which is located a brushless servomotor (Parker NV3010EAW) reaching a rotating velocity of 12 000 rpm with a nominal torque of 1.8 $N.m$. This motor drives in rotation a shaft of length 182 mm and of diameter, D, equal to 10 mm. This shaft rotates within two stationary bearings of axial length, L, of 16 mm with an order of magnitude of the nominal radial clearance of 5 μm. The bearing ratio L/D is 1.6 [13].

Two oil columns, each containing few $100mL$, feed the bearings by gravity. The temperature of the oil reservoir, close to the bearing area of interest (see inset Figure 1), is measured using four temperature probes (K-type thermocouple, TC Direct). They were placed on each side of the bearing due to the limited space within the bearing.

The friction torque is measured for the two bearings via a torquemeter Magtrol TM303 up to 0.5 $N.m$ with a resolution of 5.10^{-4} $N.m$, located between the motor and the first journal bearing.

To ensure the oil supply of the bearings without additional friction, *viscoseal* dynamic sealing with helicoïdal grooves was used on each side of the bearing.

The description of the Osiris tribometer is presented in Figure 1.

Images/Banc_OSIRIS_rogne.pdf

Figure 1: *Schematic of the Osiris tribometer. The inset shows a zoom of the bearing. The various sensors of the tribometer are also indicated.*

2.2. Film thickness measurement

2.2.1. Shaft position

To follow the position of the shaft during an experiment, six capacitive sensors from Fogale were located along the shaft. Due to space restrictions, these sensors were positioned between the two bearings. They were organized by pairs, at 90° from each other, perpendicular to the shaft axis and in three separate measurement planes [9]. The measurement range is 0-300 μm with a resolution of 3.10^{-3} μm. The acquired signal is a voltage 0-10 V proportional to the distance at a maximum frequency of $10kHz$.

2.2.2. Film thickness and cavitation zone

In order to access the film thickness distribution within the bearing, one bearing was instrumented with 12 ultrasonic sensors provided by Tribosonics Ltd. distributed uniformly along its circumference as shown in Figure 2. These sensors consist in piezoelectric elements working as transmitter and receiver of ultrasonic waves at a frequency of $1kHz$. Based on the interface stiffness methodology [14][15], they allow one to measure oil film thickness ranging from 0.1 to 50 μm (provided the appropriate calibration) and its distribution as well as to detect the existence of the cavitation zone.

2.3. Monitoring and acquisition

Commercial software such as Torque7 and xSCAN Configurator were used to acquire torquemeter and ultrasonic sensors signals. In addition, a LabVIEW software was developed to control the motor and acquire data from the motor, the thermocouples and the capacitive sensors. All data were acquired with four channel cards from National Instruments NI 9239 and NI9210. A synchronization of all the signals was performed at the onset of rotation of the shaft.

3. MEASUREMENT AND RESULTS

In the following part, typical experimental results and the tribometer validation are presented. They were ob-

ACCEPTED MANUSCRIPT
Review of Scientific Instruments
AIP Publishing
This is the author's peer reviewed, accepted manuscript. However, the online version of record will be different from this version once it has been copyedited and typeset.
PLEASE CITE THIS ARTICLE AS DOI: 10.1063/5.0155813

Figure 2: *Schematic of the ultrasonic sensors distributed along the bearing*

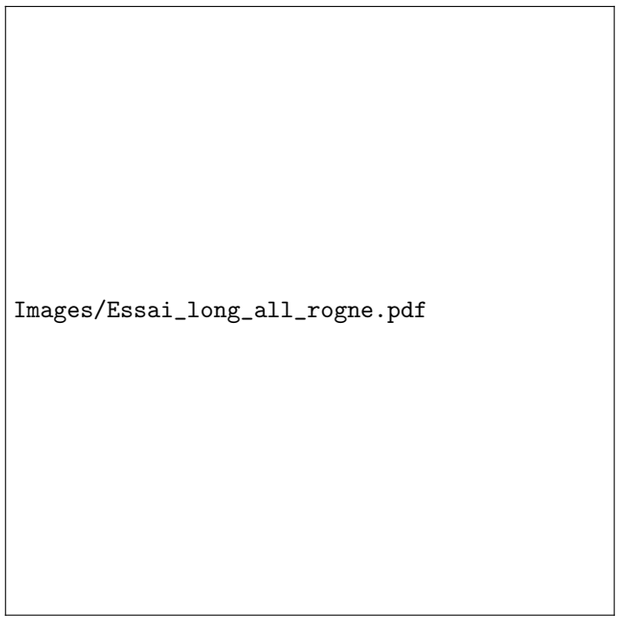

Figure 3: *Typical evolution of the torque and of the variation of temperature in the oil reservoir as a function of the velocity for an acceleration of 0.063 $m.s^{-2}$ followed by a velocity plateau at 1.57 $m.s^{-1}$ before a deceleration, for a base oil of initial viscosity η = 26.8 $mPa.s$ at 25°C and a smooth shaft (a) and zoom on the acceleration phase (b).*

tained for a group III+ base oil of low viscosity, $\eta = 26.8 mPa.s$ at $25°C$ and a smooth shaft. The radial clearance was 5.38 μm. The experimental protocol consisted in a ramp of acceleration until a target rotating velocity, which is kept constant for around $1h30$, and finally a ramp of deceleration. All the experiments were performed at least twice.

3.1. Frictional and thermal response of a sheared fluid film

Illustrative experiments were carried out at an acceleration of 0.063 $m.s^{-2}$ until the target velocity of 1.57 $m.s^{-1}$ (3000 rpm) that was maintained constant for $1h30$ before decelerating at 0.063 $m.s^{-2}$. Figure 3.a presents the evolution of the measured torque and oil column temperature as a function of the time for this controlled kinematics. At the onset of the shaft rotation, a peak of torque was detected as shown in Figure 3.b. The value of this peak results from the movement of the shaft, lifted away from the bearing surface. During the acceleration phase, the torque increases with the velocity. A maximum torque is measured once the target velocity is reached, before a decrease in torque during the constant velocity step until a steady-state torque value. The simultaneous variation of the oil column temperature shows that the temperature is quasi constant, $+0.2°C$, during this acceleration phase. It increases then dramatically of $7°C$ during the constant velocity step.

3.2. Validation of the tribometer

In order to validate the tribometer and especially the torque values, experiments were performed for a step of constant velocity. The value of the constant velocity varied up to 3.67 $m.s^{-1}$ (7000 rpm). The values of the maximum torque, measured at the end of the deceleration phase and of the steady-state torque, measured at the end of the constant velocity step, were plotted vs the velocity - see Figure 4.a and .b.

In a first qualitative approach to validate the hydrodynamic friction set-up, one can consider that, for a centred shaft in the bearing, neglecting the existence of cavitation, the viscous flow follows a Couette flow. It is then possible to calculate the shear stress and the torque as a function of the viscosity. The shear stress is:

$$\tau = \frac{\eta.U}{C_r} \tag{1}$$

with U the shaft velocity and C_r the radial clearance.

The torque in one bearing can then be calculated as follows:

$$C = \frac{2\pi.\eta.U.D^2.L}{4.C_r} \tag{2}$$

ACCEPTED MANUSCRIPT
Review of Scientific Instruments
AIP Publishing
This is the author's peer reviewed, accepted manuscript. However, the online version of record will be different from this version once it has been copyedited and typeset.
PLEASE CITE THIS ARTICLE AS DOI: 10.1063/5.0155813

During the acceleration phase, the torque measured for two bearings increases linearly with the velocity as predicted by equation 2.

The theoretical maximum torque was calculated by assuming an athermal process during the acceleration phase and therefore a fluid viscosity equal to the one at $25°C$. These values of torque were compared to the measured experimental ones in Figure 4.a. The values remain of the right order of magnitude. The agreement between the two values is perfect below a velocity of 1.57 $m.s^{-1}$. Above this velocity, the theoretical values diverge from the measured ones. One can assume that thermal effects, neglected at first, generated during the slow increase in velocity at an acceleration of 0.063 $m.s^{-2}$, can explain the decrease in viscosity and the diminution of the measured viscous torque.

In the case of the steady-state torque value, the increase in temperature in the reservoir and the associated decrease in viscosity, were taken into account during each constant velocity step, assuming that the variation of temperature in the reservoir was representative of that in the bearing. The evolution of the theoretical and measured steady-state torques follows the same trend with the increase in velocity (see Figure 4.b). Once again, the calculated values are larger than the measured ones, despite being of the same order of magnitude. This could be explained by a small difference in temperature between the reservoir and the bearing and/or the non-centred shaft and/or the existence of a cavitation zone.

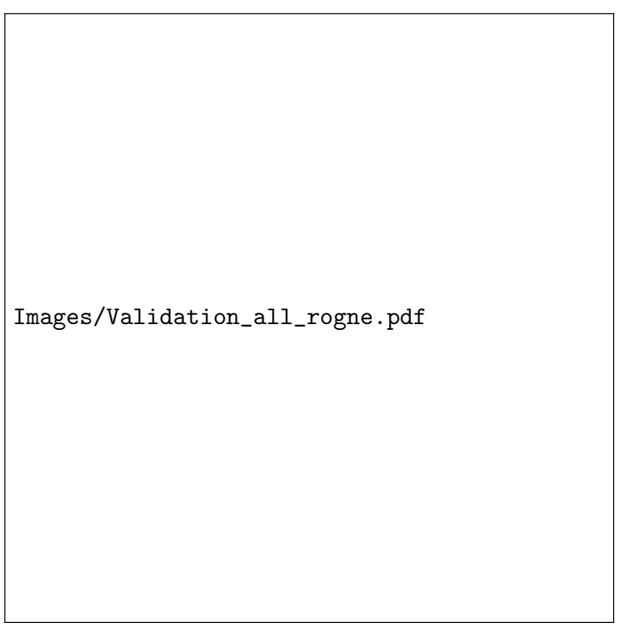

Figure 4: *Comparative evolution of the maximum torque (a) and of the steady-state torque (b) versus velocity between measured and theoretical values, assuming a Couette flow without cavitation.*

3.3. Role of the velocity: thermal effects

To highlight the thermal effects on the friction response of the fluid film, the velocity was varied. Experiments were performed with the same acceleration value until a target velocity of either 1.57 or 3.67 $m.s^{-1}$, that was maintained for a step of $1h30$. Figure 5 shows the evolution of the torque and of the temperature variation with time. The torque evolution remains similar. During the acceleration phase, the torque values superimpose perfectly. During the constant velocity step, the torque values are superior at higher velocity, in agreement with equation 2. It can be seen that the torque strongly decreased in the first $10 minutes$ of the experiment as 70% of the final value was attained. However, the variation of temperature differs as a function of the time during this velocity plateau: the variation of temperature reached $18°C$ at the highest velocity, compared to $7°C$ at 1.57 $m.s^{-1}$. Although the temperature is not stabilized at the end of the steady-state regime velocity, it can be seen that the temperature strongly increased in the first $10 minutes$ of the experiment as 60-70% of the final value was attained. This evolution is also in agreement with the stabilization of the torque values. We confirm here that shearing the thin fluid film at higher velocity increases the thermal dissipation as expected.

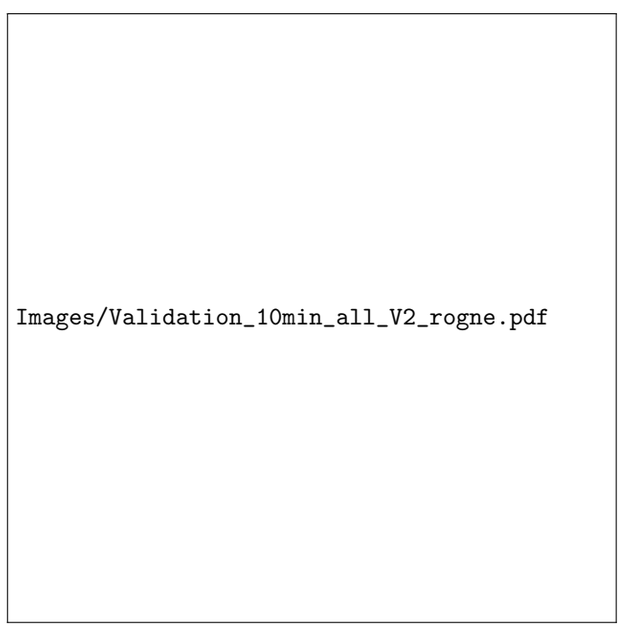

Figure 5: *Influence of the velocity on the evolution of the torque (a) and of the variation of temperature in the oil column (b) versus time.*

In the following parts, this time duration of 10 $minutes$ and the target velocity of 3.67 $m.s^{-1}$ (7000 rpm) was chosen.

ACCEPTED MANUSCRIPT
Review of Scientific Instruments
AIP Publishing
This is the author's peer reviewed, accepted manuscript. However, the online version of record will be different from this version once it has been copyedited and typeset.
PLEASE CITE THIS ARTICLE AS DOI: 10.1063/5.0155813

3.4. Role of the acceleration: thermal and inertia contribution

In this paragraph, only the effect of the acceleration phase was investigated on the temperature variation evolution and the torque. The acceleration was varied from 0.031 to 15.7 $m.s^{-2}$ up to a velocity of 3.67 $m.s^{-1}$. Depending on the acceleration, the variation of temperature could reach $3.4°C$ at the slowest acceleration as shown in Figure 6, indicating that the acceleration phase is only purely athermal for acceleration above 1.57 $m.s^{-2}$.

Figure 6: *Influence of the acceleration on the evolution of the variation of temperature in the oil column up to a velocity of 3.67 $m.s^{-1}$.*

The corresponding torque evolution clearly indicates a strong dependence with the acceleration (see Figure 7): the torque values were shifted to higher values as the acceleration increases.

This was the signature of the inertia contribution of the mechanical parts at the onset of rotation. The inertia contribution was also visible during the experiment at the end of acceleration and at the onset of deceleration: a sudden drop of the torque was detected. The values of the drop were similar at these two instants, depending mainly on the acceleration/deceleration value. In order to fully characterize the inertia contribution, the values of the inertial torque measured experimentally (averaged on the two values measured at each drop for each experiment) were compared to the calculated value, as a function of the acceleration, and reported in table I. The theoretical values were calculated with:

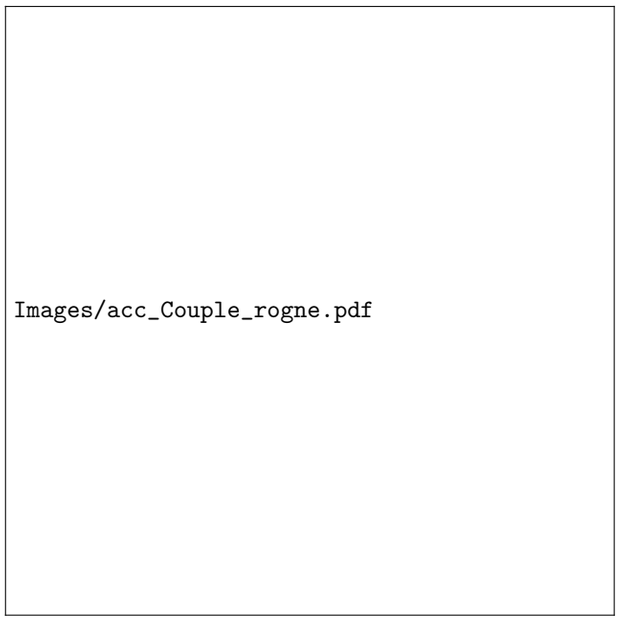

Figure 7: *Influence of the acceleration on the evolution of the torque up to a velocity of 3.67 $m.s^{-1}$.*

$$C_i = \frac{\omega.I}{\delta t} \tag{3}$$

where C_i is the inertial torque, I is the inertia of the system taking into account the rotating mechanical elements equal to 553 $g.cm^2$, ω the angular velocity and δt the duration of the acceleration phase.

Acceleration ($m.s^{-2}$)	Measured inertial torque C_i ($mN.m$)	Calculated inertial torque C_i ($mN.m$)
0.031	0.19 ± 0.02	0.18
0.063	0.23 ± 0.03	0.35
0.31	1.6 ± 0.1	1.7
1.57	8.4 ± 0.9	8.9
3.14	16.4 ± 1.7	17.9
6.28	34.4 ± 3.5	35.8
15.7	80.1 ± 8.0	89.6

Table I: *Comparison between the measured and calculated inertial torque C_i as a function of the acceleration*

A good agreement was obtained between the calculated values and the ones measured experimentally. The small discrepancy was attributed to geometrical errors. This analysis confirms that the drop in torque, observed experimentally, resulted from the inertia.

ACCEPTED MANUSCRIPT
Review of Scientific Instruments
AIP Publishing
This is the author's peer reviewed, accepted manuscript. However, the online version of record will be different from this version once it has been copyedited and typeset.
PLEASE CITE THIS ARTICLE AS DOI: 10.1063/5.0155813

3.5. In situ analysis of the film forming mechanisms

3.5.1. Eccentricity analysis

Using the six capacitive sensors gives access to the position of the shaft compared to the bearing, in each measurement plane. Knowing the relative distance from the sensor to the shaft surface, in two points M and N, the position of the center $O(a, b)$ of the shaft is given by:

$$a = \frac{X_M}{2} - \frac{Z_N}{2}.\sqrt{\frac{D^2 - {X_M}^2 - {Z_N}^2}{{X_M}^2 + {Z_N}^2}} \tag{4}$$

$$b = \frac{Z_N}{2} - \frac{X_M}{2}.\sqrt{\frac{D^2 - {X_M}^2 - {Z_N}^2}{{X_M}^2 + {Z_N}^2}} \tag{5}$$

This allows one to calculate and plot the orbits of movement of the shaft center. The orbits present a specific shape related to each couple shaft-bearing due to geometrical defects as well as possible misalignment. These measurement artefacts can be eliminated by an adequate frequency filtering. A bandpass filter was used to isolate the main frequency, representative of the shaft rotation. These orbits exhibit different amplitudes in each measurement plane, indicating that the shaft was deformed during the rotation (see Figure 8.a).

Assuming a polynomial extrapolation of second order as proposed in [9], it is then possible to determine the position of the shaft center, along the shaft length, and therefore in the bearings. Figure 8 presents the extrapolated 3D orbit of the shaft. The amplitude varies in each bearing, due to the presence of a mechanical coupling with the motor and the torquemeter: this limits the movement amplitude in the first bearing (see inset c) compared to the second one. This strong initial assumption offers the advantage of an easily-obtained qualitative information regarding the shaft position.

This analysis provides the evolution of the shaft position as a function of time during the experiment. The film thickness, h, can then be calculated:

$$h = C_r.(1 + \epsilon.cos\theta) \tag{6}$$

with ϵ the relative eccentricity and θ a given angle. Figure 9 presents the evolution of the mean and maximal eccentricity and of the corresponding minimum film thickness in the mid-plane of bearing 1. At first, the eccentricity decreases, indicating the lift of the shaft. Once the constant velocity step reached, the eccentricity decreases again, representing the centering of the orbits in the bearings, before stabilization. It remains constant for the rest of the steady-state regime. The film thickness evolution is directly correlated to the eccentricity evolution.

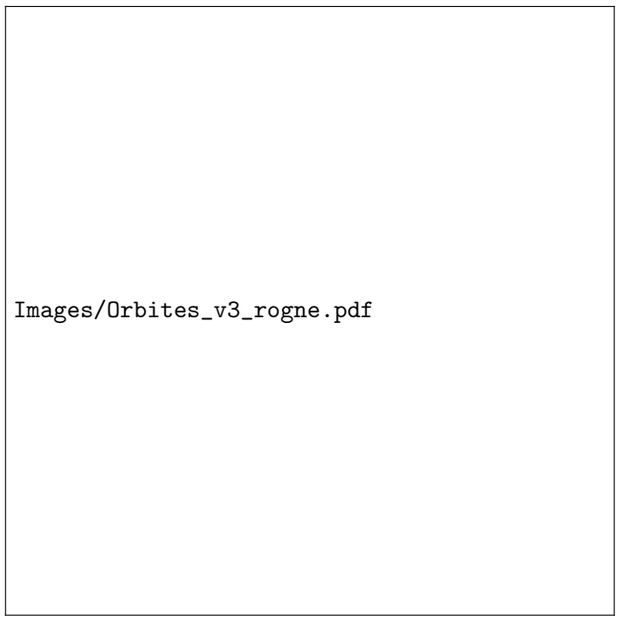

Figure 8: *(a) 3D orbit extrapolated from the positions of the shaft center at the end of the steady-state regime. The three measurement planes are represented as well as the instrumented bearing on left and the bearing 2 on the right. The inset (b) represents the measurement before and after filtering in the second measurement plane. The inset (c) shows the extrapolated orbits of the shaft center in the instrumented bearing.*

This first rough analysis does not account for the existence of cavitation.

3.5.2. Film thickness distribution and cavitation zone localization

In order to better estimate the film thickness distribution, ultrasonic sensors were used. Nevertheless, an accurate measurement of the film thickness itself, based on the interface stiffness methodology developed by [14][15], requires a calibration with neither the shaft, nor the oil to define the reference in film thickness. In addition, the evolution of the wave propagation velocity in the fluid (for each fluid) as a function of the temperature as well as the acoustic impedance of the solids need to be known. In this context, the ultrasonic sensors were here only used to detect the presence of cavitation in the bearing and to determine its extension.

The estimate of the cavitation zone position and extension can be performed with a accuracy of 30° as a result of the geometrical distribution of the twelve sensors along the bearing circumference. During the steady-state regime, at constant velocity, the orbits can be considered as stable and constant. A relative variation of the mean film thickness can be qualitatively detected and trans-

ACCEPTED MANUSCRIPT
Review of Scientific Instruments
AIP Publishing
This is the author's peer reviewed, accepted manuscript. However, the online version of record will be different from this version once it has been copyedited and typeset.
PLEASE CITE THIS ARTICLE AS DOI: 10.1063/5.0155813

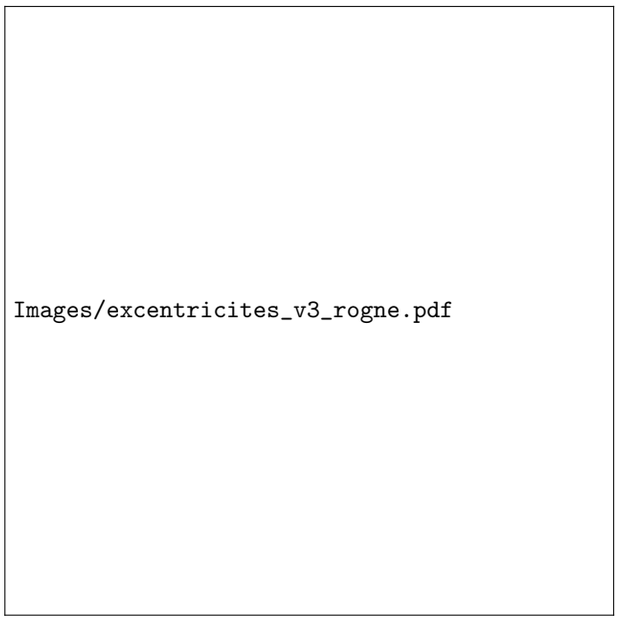

Figure 9: *Time evolution of the mean and maximum eccentricity as well as the minimum film thickness, calculated within the instrumented bearing.*

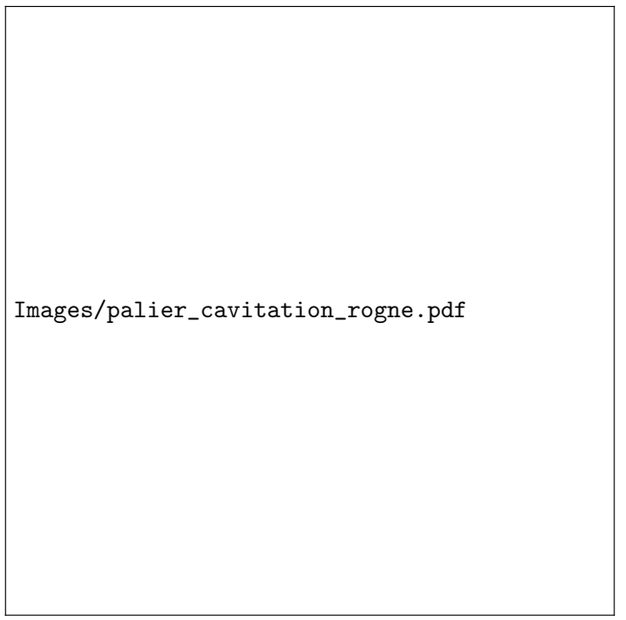

Figure 10: *Example of localization of the cavitation zone and estimate of its extension at the end of the steady-state regime in the instrumented bearing.*

lated in three different relative levels of thickness defined as $+$, $+-$ and $-$. Each sensor providing one level, the distribution of the film thickness can be extrapolated along the circumference of the bearing. Knowing the direction of rotation and considering the position of the shaft where the maximum of the eccentricity is achieved, the cavitation zone can then be estimated and localized, in the contact divergent (see Figure 10 for instance, corresponding at a time of 572 s in steady-state regime at a constant velocity of 3.67 $m.s^{-1}$.

This analysis provides an approximate evolution of the cavitation zone extension as a function of the time as shown in Figure 11 in the first bearing. The extension of the cavitation zone seems to increase at first, before decreasing and reaching a stable value after 300 s. From the instantaneous estimate of the shaft position and the cavitation length, the inlet zone can be deduced.

4. CAPABILITY TO DETECT SURFACE EFFECTS

4.1. Influence of the surface texturing on the friction and cavitation extension

In order to demonstrate the capability of the Osiris tribometer, experiments with femtosecond LASER-textured surfaces with a cavity density of about 15% and cavity 2 μm deep were performed at a target velocity of 3.67 $m.s^{-1}$ and an acceleration of 0.31 $m.s^{-2}$. An increase of 8% in friction torque was detected compared to the one measured for the smooth surface, associated with a diminution of the cavitation length extension as shown in Figure 12. The maximum eccentricity ratio increased at 0.4 for the considered textured surface while it was about 0.2 for the smooth surface.

4.2. Influence of the oil formulation

Formulated oils of viscosity around $40mPa.s$ were also tested on smooth surfaces. The extension of the cavitation length was impacted by the presence of the poly(alkyl)metacrylate additives known to adsorb on the surfaces to form boundary layers [16]: a decrease in the cavitation length of 30° was measured compared to those measured with base oil (see Figure 12). In parallel, the friction torque slightly increased. These results confirmed the capability of the Osiris tribometer to detect surface effects even in hydrodynamic lubrication regime.

5. SUMMARY

This Osiris model tribometer working in thin film conditions and hydrodynamic lubrication regime combines simultaneous friction and in situ measurements of shaft position, film thickness distribution, localization and extension of the cavitation zone and temperature for a controlled contact kinematics. The nominal radial clearance was about 5 μm. The validation of the tribometer was perfomed by confronting the measured friction torque

ACCEPTED MANUSCRIPT
Review of Scientific Instruments
AIP Publishing
This is the author's peer reviewed, accepted manuscript. However, the online version of record will be different from this version once it has been copyedited and typeset.
PLEASE CITE THIS ARTICLE AS DOI: 10.1063/5.0155813

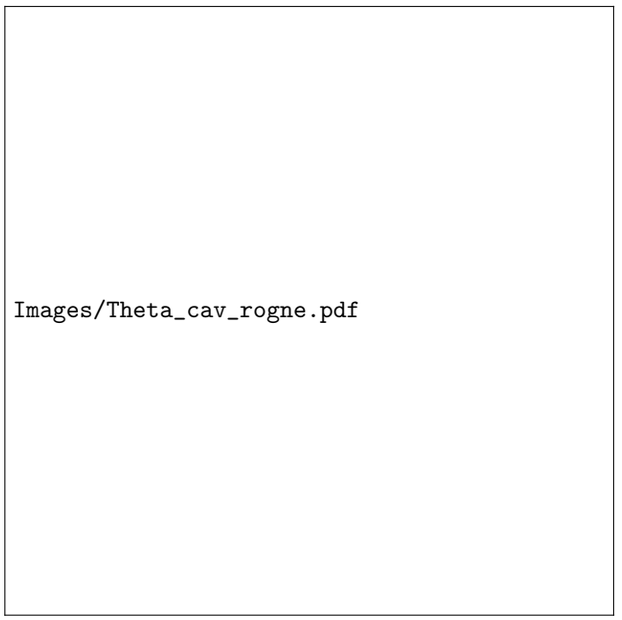

Figure 11: *Cavitation length estimated as a function of time in the instrumented bearing.*

values up to 0.5 $N.m$ to calculated ones, using a simplified framework of assumptions.

By changing the velocity up to 4 $m.s^{-1}$ and the controlled acceleration up to 16 $m.s^{-2}$ $m.s^{-2}$, we were able to discriminate and discuss the thermal and the inertial relative contributions. The latter was further validated by a comparison with theoretical values of inertial torque. To further analyze the in situ mechanisms within the bearing, capacitive sensors and their associated geometrical analysis provided the extrapolated position of the shaft and allowed one to deduce the eccentricity. The minimum film thickness was therefore calculated in the bearing. The film thickness distribution was analyzed and the cavitation localization and extension were estimated with a resolution of 30°.

Finally, the Osiris ability to detect low friction and small variation of friction induced by surface effects was demonstrated by performing tests with textured surfaces. We illustrated in this example that the length of the cavitation zone was reduced resulting in an increase in friction torque. We also highlighted the role of the fluid formulation with the existence of an adsorbed boundary layer on the surface that modified the extension of the cavitation zone.

This apparatus showed its capability to detect small variation in friction correlated with film thickness distribution and shaft position, opening innovative research path for coating and texturing development as well as low viscosity fluid formulation such as environmentally-friendly aqueous lubricants. An advantage of this tribometer is the need of small volumes of fluid. In addition, the in situ measurements provide input data for numerical simulations in order to improve the understanding of the hydrodynamic lubrication mechanisms, especially in thin film conditions and with textured surfaces.

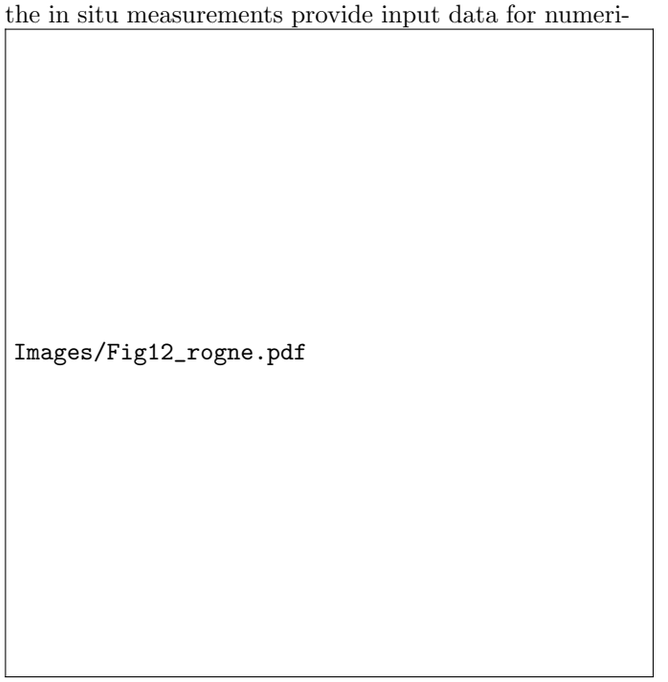

Figure 12: *Cavitation length estimated as a function of time in the instrumented bearing for a textured surface compared to the smooth one for a base oil and for a formulated oil with a smooth surface.*

Acknowledgments

This research was financially supported by the ADEME, the French Agency for the ecological transition, via the IMOTEP project.

[1] J. Frene *Butées et Paliers Hydrodynamiques* (Techniques de l'Ingenieur, 1995)
[2] G. W. Stachowiak and A. W. Batchelor *Engineering Tribology* (Elsevier, 3rd edition, 2005)
[3] M. M. Khonsari and E. R. Booser *Applied Tribology: Bearing Design and Lubrication* (Wiley, 3rd edition, 2017)
[4] P. D. Swales *A Review of Cavitation Phenomena in Engineering Situations* (In C. M. Taylor et al editors, Proceedings of the 1st Leeds-Lyon Symposium in Tribology,

ACCEPTED MANUSCRIPT
Review of Scientific Instruments
AIP Publishing
This is the author's peer reviewed, accepted manuscript. However, the online version of record will be different from this version once it has been copyedited and typeset.
PLEASE CITE THIS ARTICLE AS DOI: 10.1063/5.0155813

3-9, 1974)

[5] D. Dowson and C. M. Taylor *Cavitation in Bearings* (Annual Review of Fluid Mechanics, 1979)

[6] M. J. Braun and W. H. Hannon *Cavitation Formation and Modelling for Fluid Film Bearings: A Review* (Journal of Engineering Tribology, 224: 839-863, 2010)

[7] R. Boncompain, M. Fillon and J. Frene *Analysis of Thermal Effects in Hydrodynamic Bearings* (ASME Journal of Tribology, 108(2): 219-224, 1986)

[8] T. Woloszynski, P. Podsiadło and G. W. Stachowiak *Efficient Solution to the Cavitation Problem in Hydrodynamic Lubrication* (Tribology Letters, 58: 1-11, 2015)

[9] J. Rebufa *Vibrations de ligne d'arbre sur paliers hydrodynamiques: influence de l'etat de surface* (PhD thesis, 2016-LYSEC44, Ecole centrale de Lyon, 2016)

[10] J. Rebufa, F. Thouverez, E. Le Guyadec and D. Mazuyer *Nonlinear Effects of Surface Texturing on the Performance of Journal Bearings in Flexible Rotordynamic Systems* (ASME. Journal of Tribology, 139(5): 051705, 2017).

[11] C. Giraudeau *Influence des discontinuités géométriques sur les performances des paliers en régime thermoélastohydrodynamique (TEHD)* (PhD thesis, Universite de Poitiers, 2016)

[12] B. Pap *Modelisation d'un palier hydrodynamique de reducteur epicycloïdal opérant en conditions severes* (PhD thesis, Universite de Poitiers, 2018)

[13] C. Barazzutti *Effets de surface sur le comportement tribologique d'un palier hydrodynamique* (PhD thesis, 2023ECDL0002, Ecole centrale de Lyon, 2023)

[14] R. S. Dwyer-Joyce, P. Harper and B. W. Drinkwater *A Method for the Measurement of Hydrodynamic Oil Films using Ultrasonic Reflection* (Tribology Letters, 17(2): 337-348, 2004)

[15] S. Kasplang and R. S. Dwyer-Joyce *Observations of Film Thickness Profile and Cavitation around a Journal Bearing Circumference* (Tribology Transactions, 51(2): 231-245, 2008)

[16] F. Abouhadid *Aspects moleculaires du frottement limite: couplage entre structure des additifs et physico-chimie des surfaces* (PhD thesis, 2021-LYSEC48, Ecole centrale de Lyon, 2021)

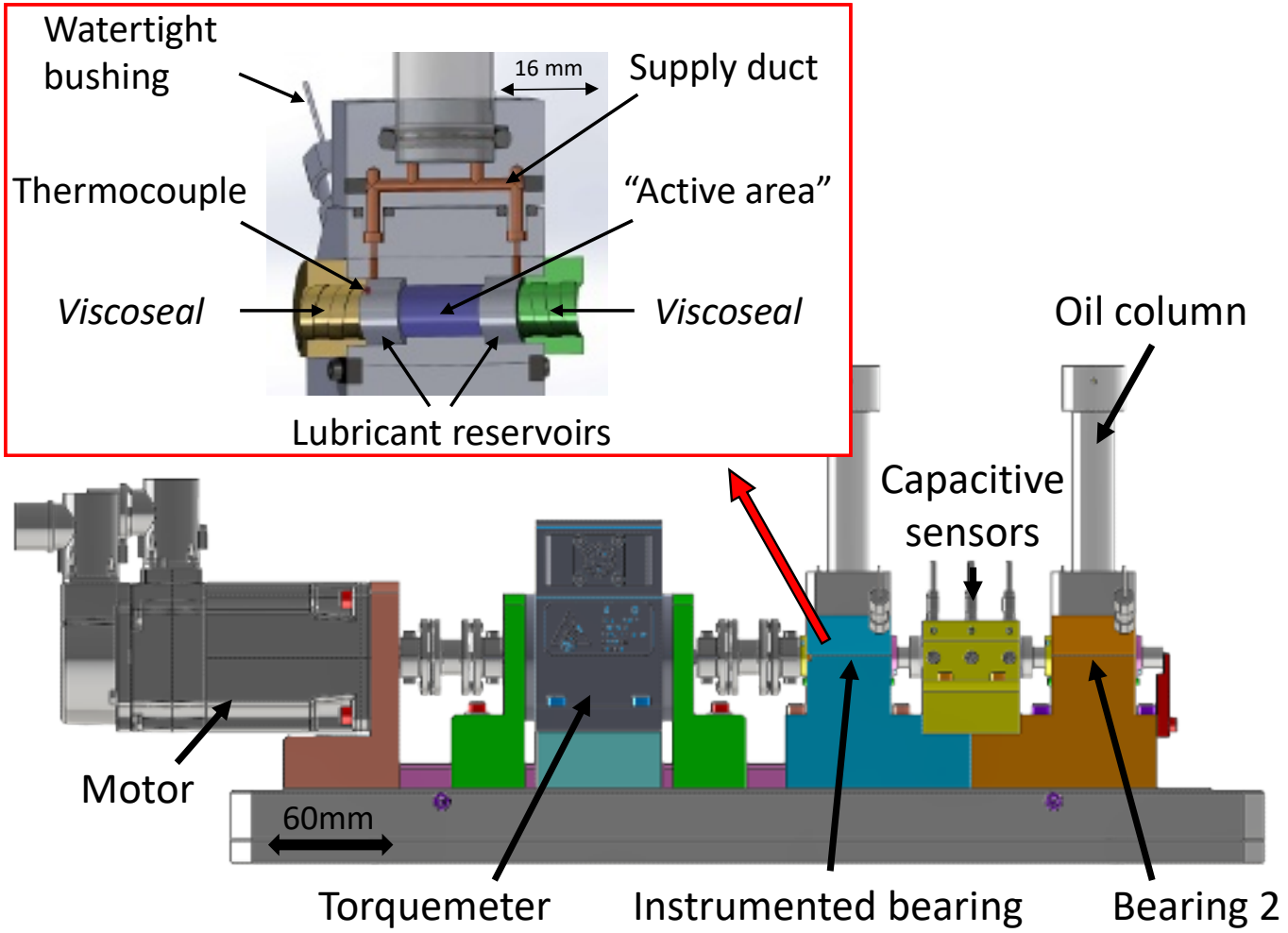
Watertight bushing
16 mm
Supply duct
Thermocouple
"Active area"
Viscoseal
Viscoseal
Lubricant reservoirs
Oil column
Capacitive sensors
Motor
60mm
Torquemeter
Instrumented bearing
Bearing 2

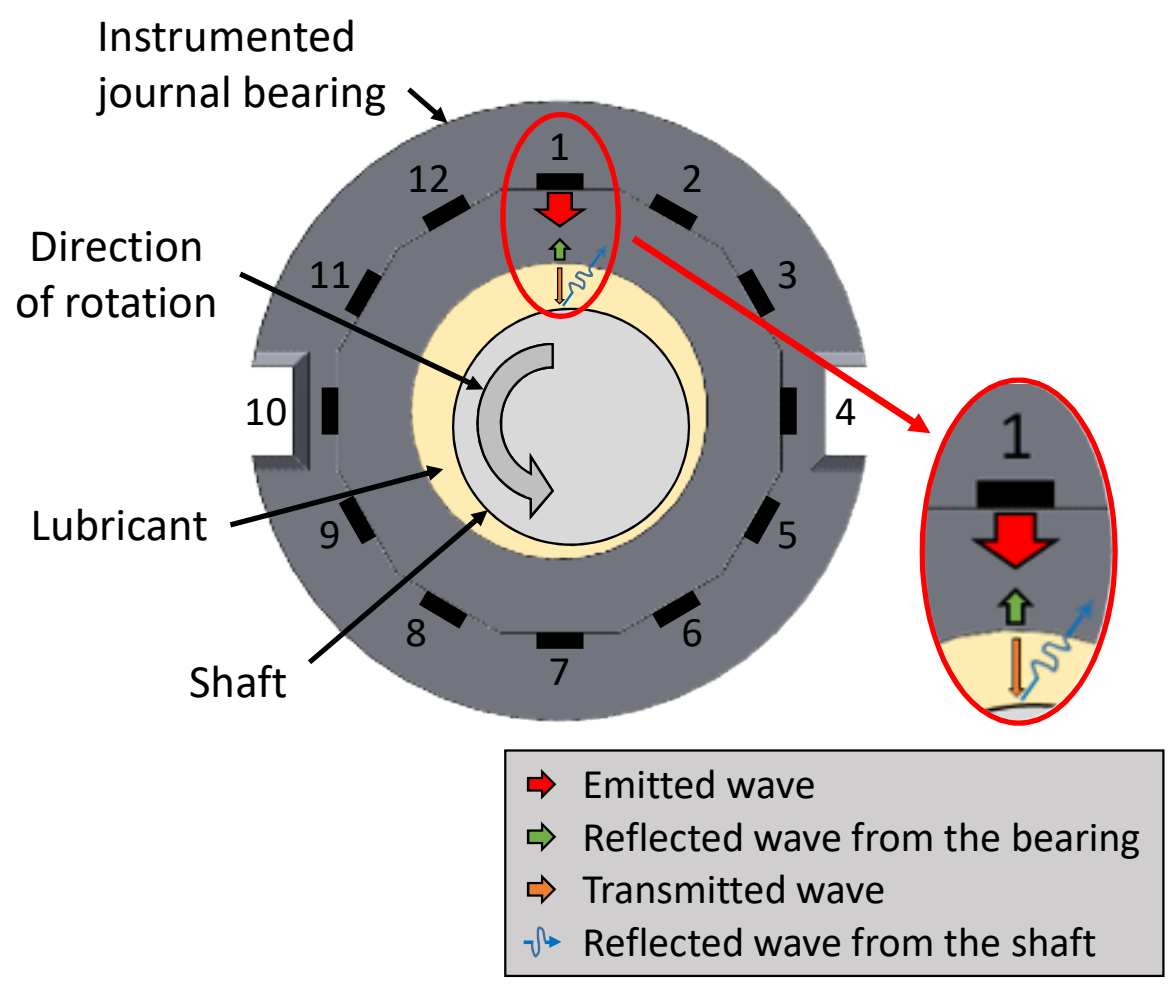
Instrumented journal bearing
Direction of rotation
Lubricant
Shaft
1
2
3
4
5
6
7
8
9
10
11
12
Emitted wave
Reflected wave from the bearing
Transmitted wave
Reflected wave from the shaft

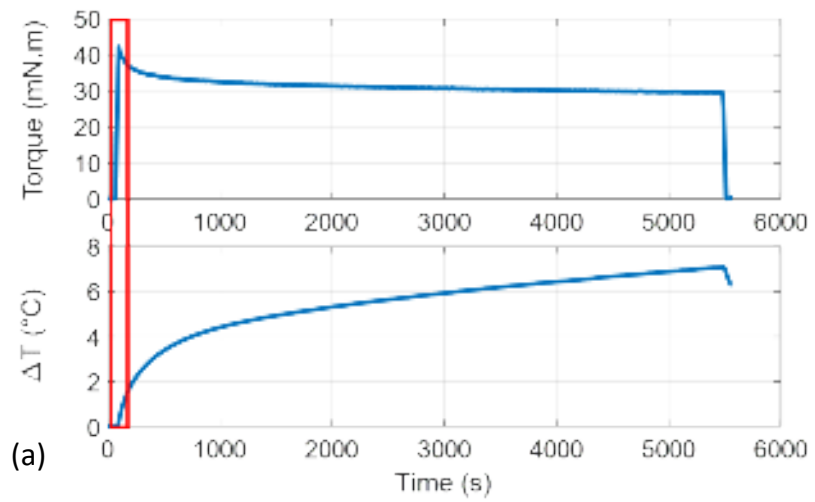
Torque (mN.m)
ΔT (°C)
Time (s)

(a)

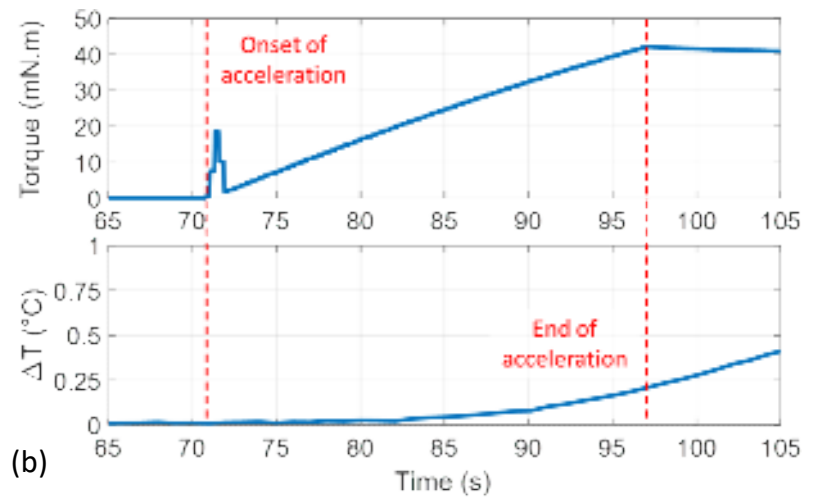
Onset of acceleration
End of acceleration
Torque (mN.m)
ΔT (°C)
Time (s)

(b)

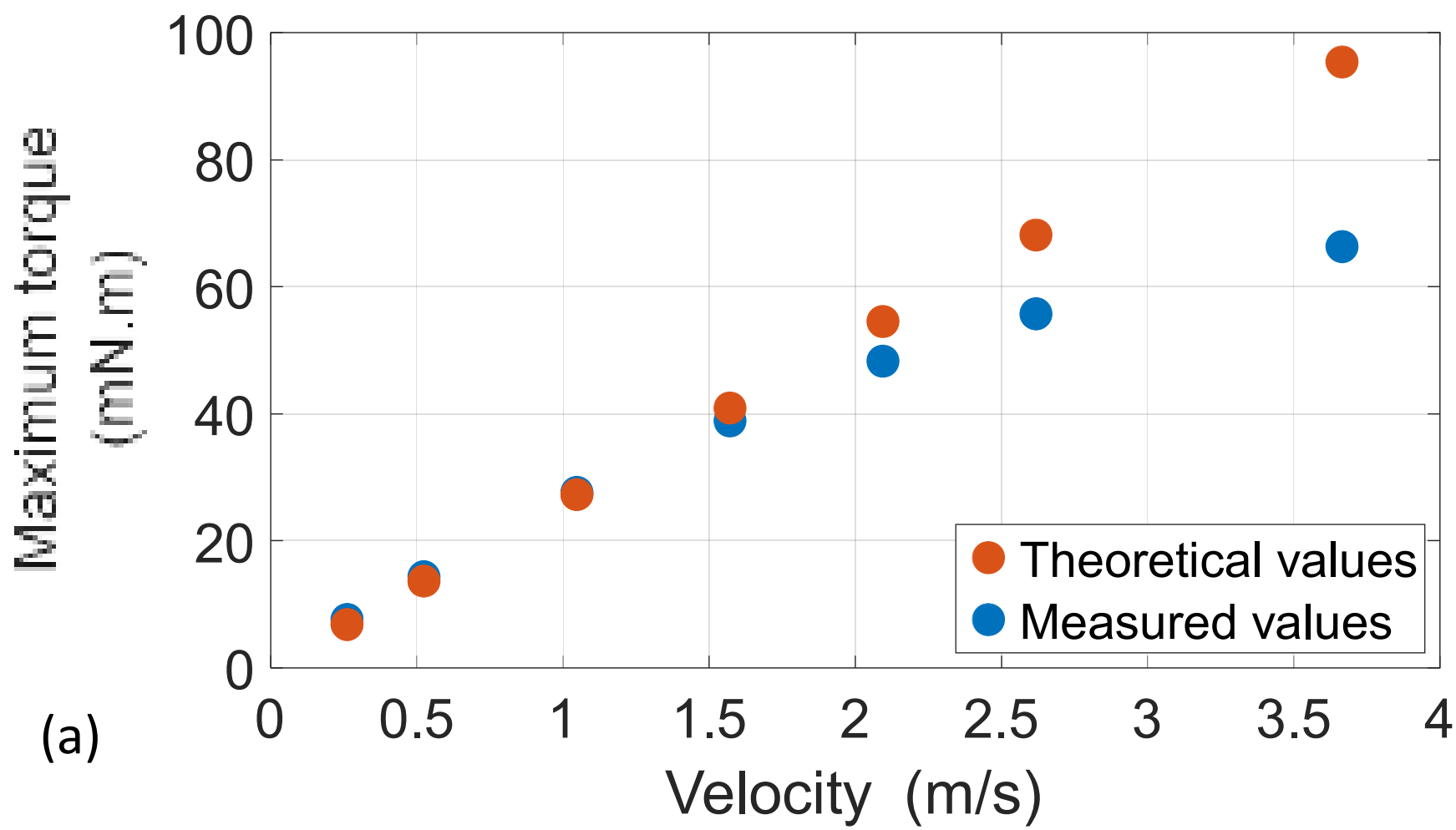
Maximum torque (mN.m)
100
80
60
40
20
0
0
0.5
1
1.5
2
2.5
3
3.5
4
Velocity (m/s)
Theoretical values
Measured values

(a)

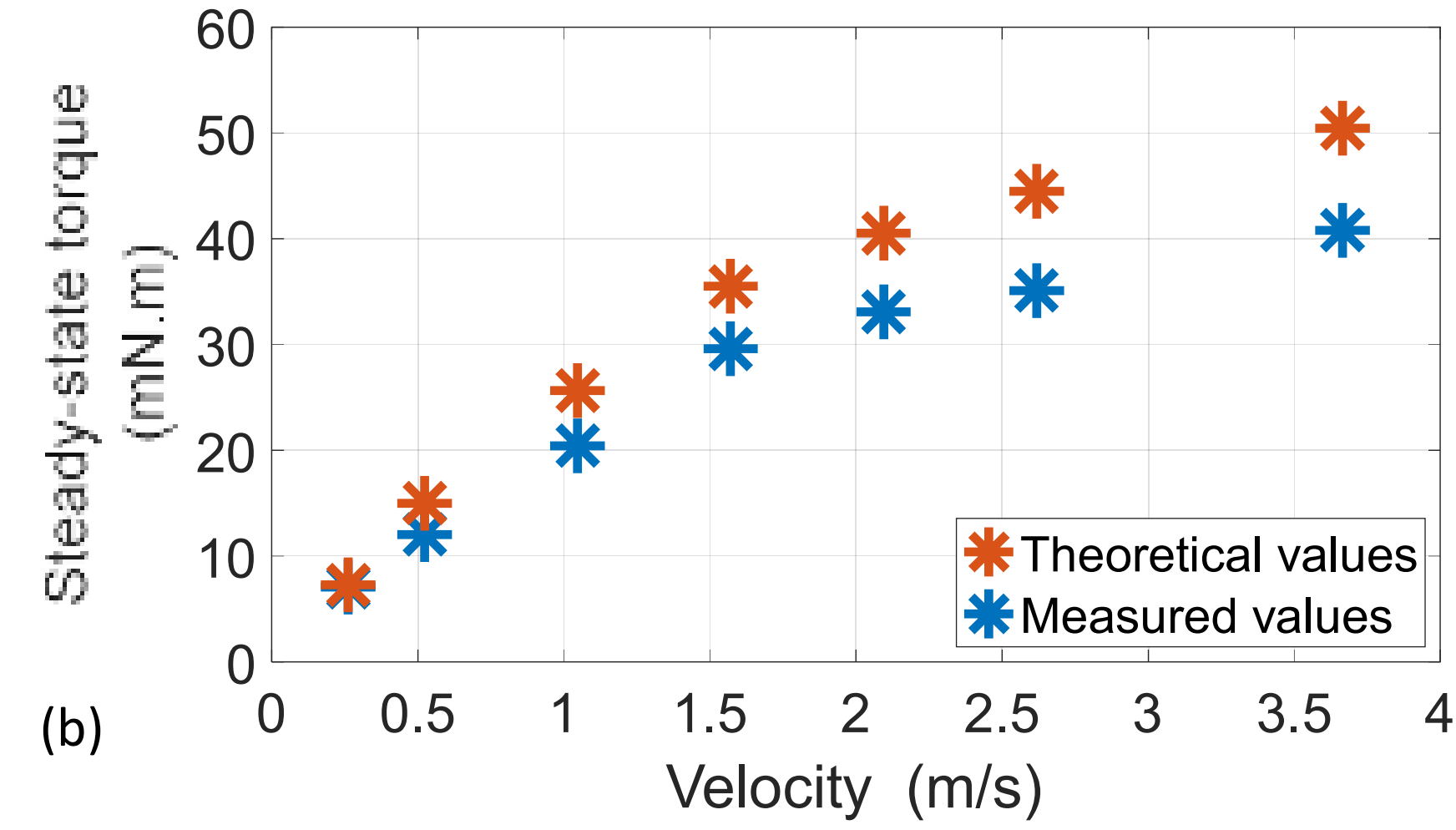
Steady-state torque (mN.m)
60
50
40
30
20
10
0
0
0.5
1
1.5
2
2.5
3
3.5
4
Velocity (m/s)
Theoretical values
Measured values

(b)

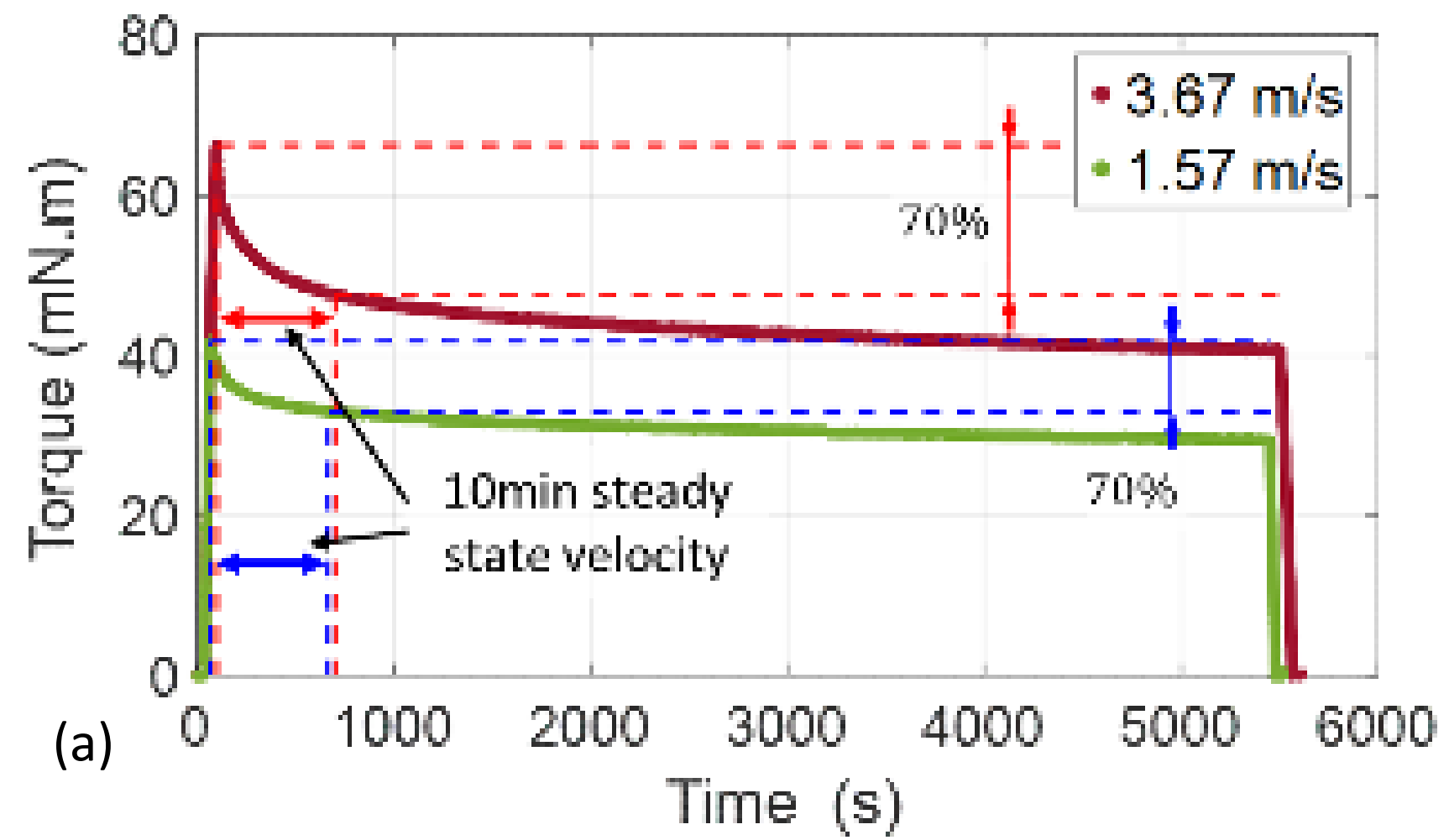
3.67 m/s
1.57 m/s
70%
70%
10min steady
state velocity
Torque (mN.m)
Time (s)
0
20
40
60
80
0
1000
2000
3000
4000
5000
6000

(a)

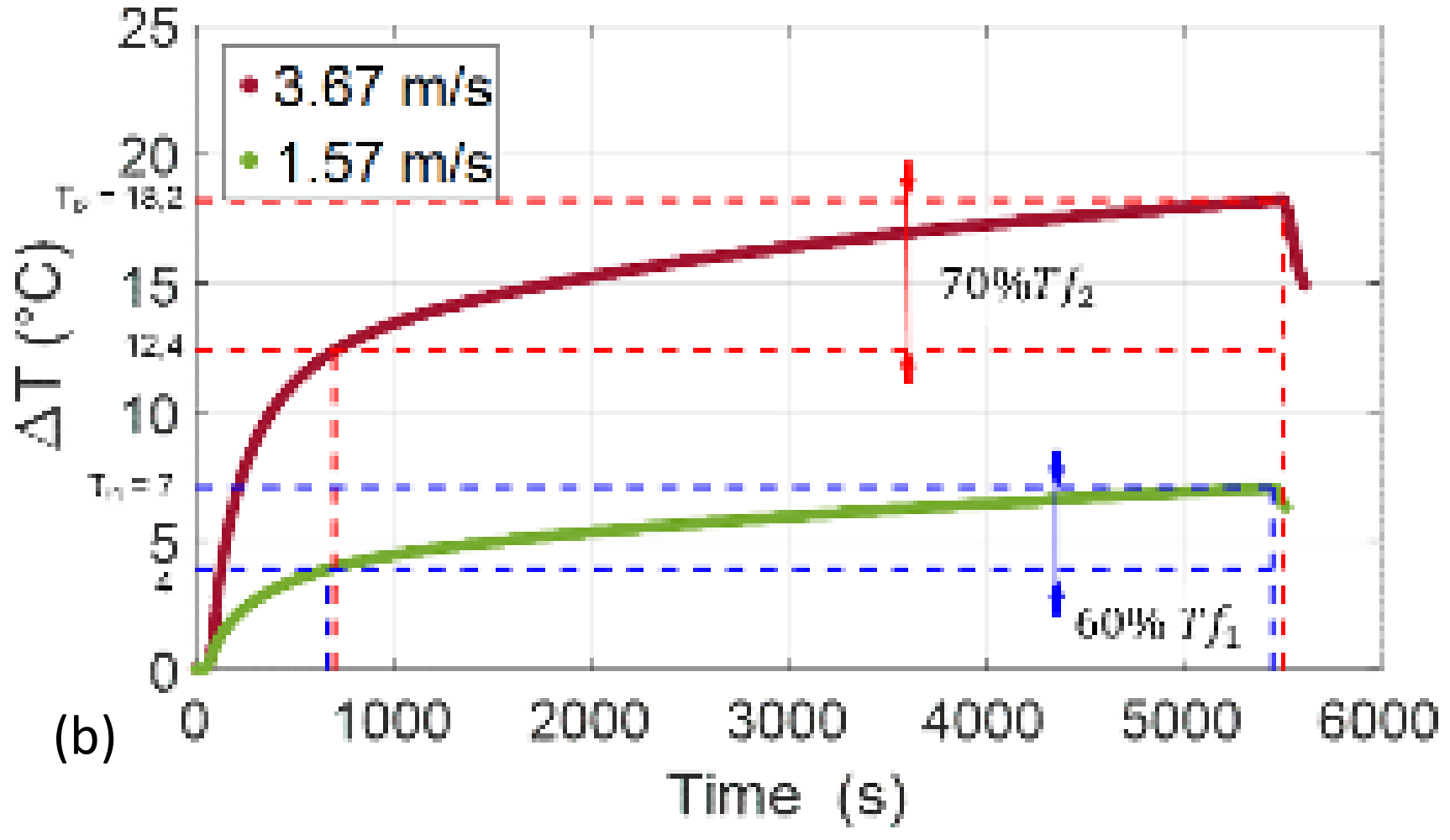
3.67 m/s
1.57 m/s
T_2 = 18,2
12,4
T_1 = 7
$70\%Tf_2$
$60\%\ Tf_1$
ΔT (°C)
Time (s)
0
5
10
15
20
25
0
1000
2000
3000
4000
5000
6000

(b)

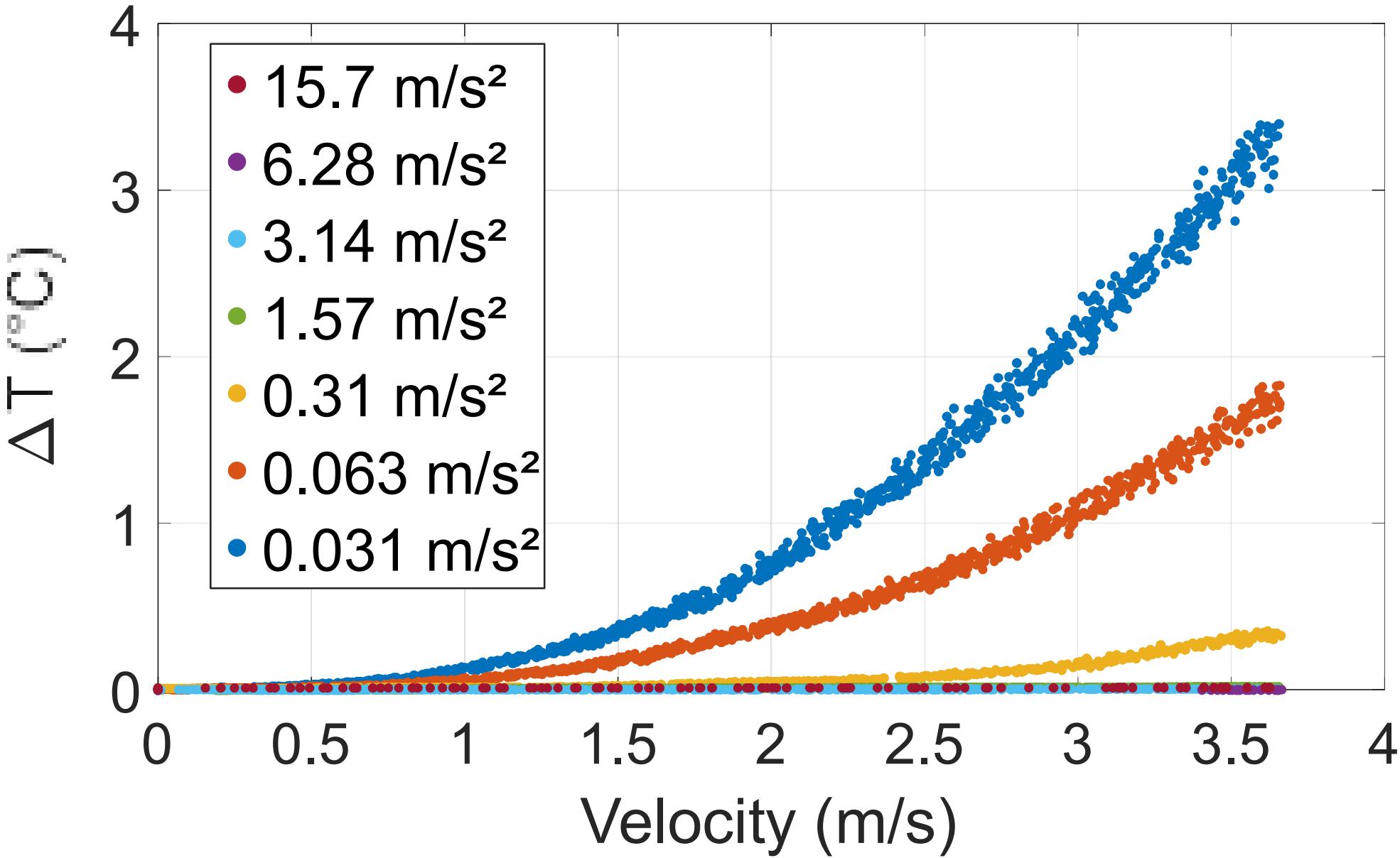
15.7 m/s²
6.28 m/s²
3.14 m/s²
1.57 m/s²
0.31 m/s²
0.063 m/s²
0.031 m/s²
ΔT (°C)
0
1
2
3
4
0
0.5
1
1.5
2
2.5
3
3.5
4
Velocity (m/s)

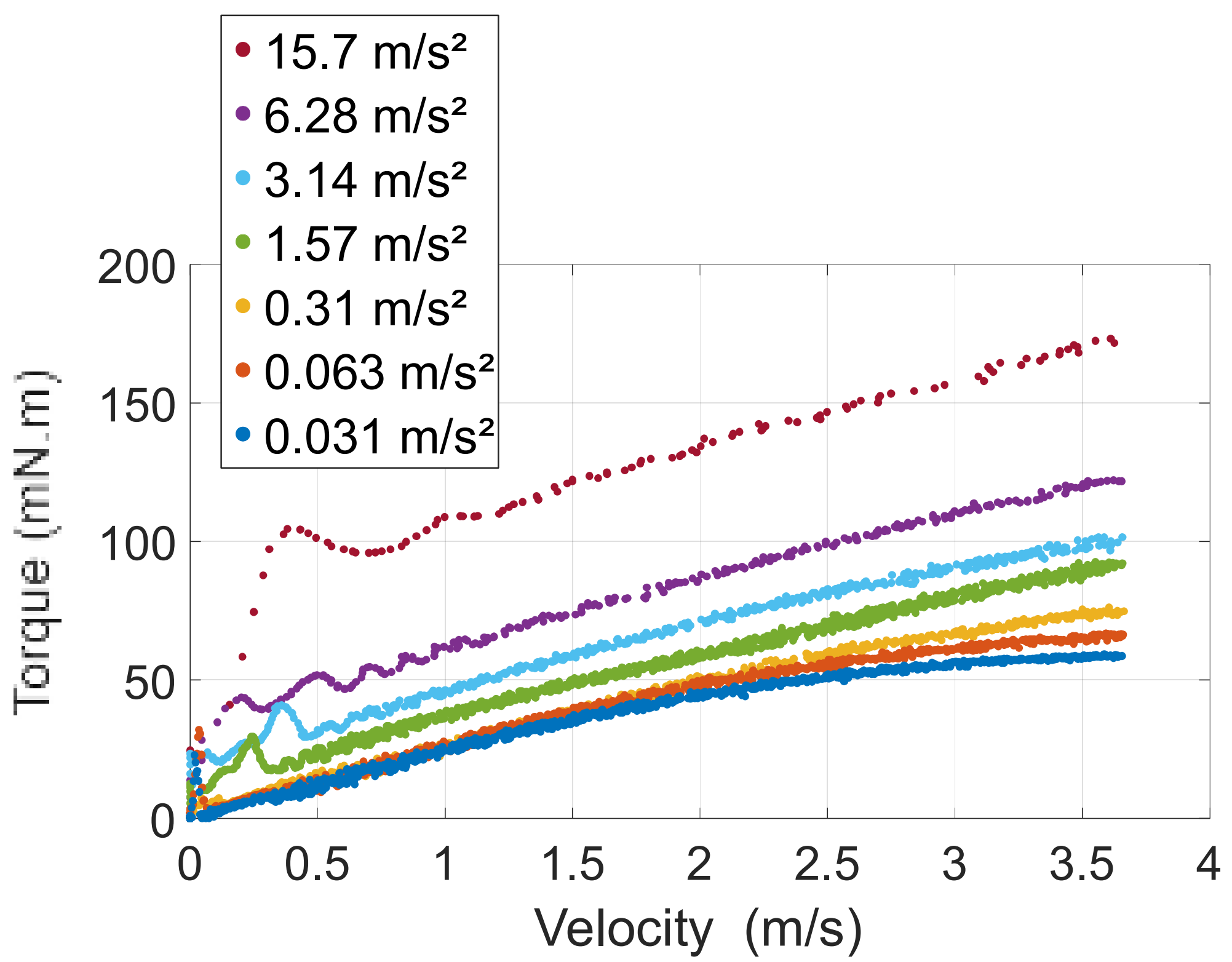
15.7 m/s²
6.28 m/s²
3.14 m/s²
1.57 m/s²
0.31 m/s²
0.063 m/s²
0.031 m/s²
200
150
100
50
0
Torque (mN.m)
0
0.5
1
1.5
2
2.5
3
3.5
4
Velocity (m/s)

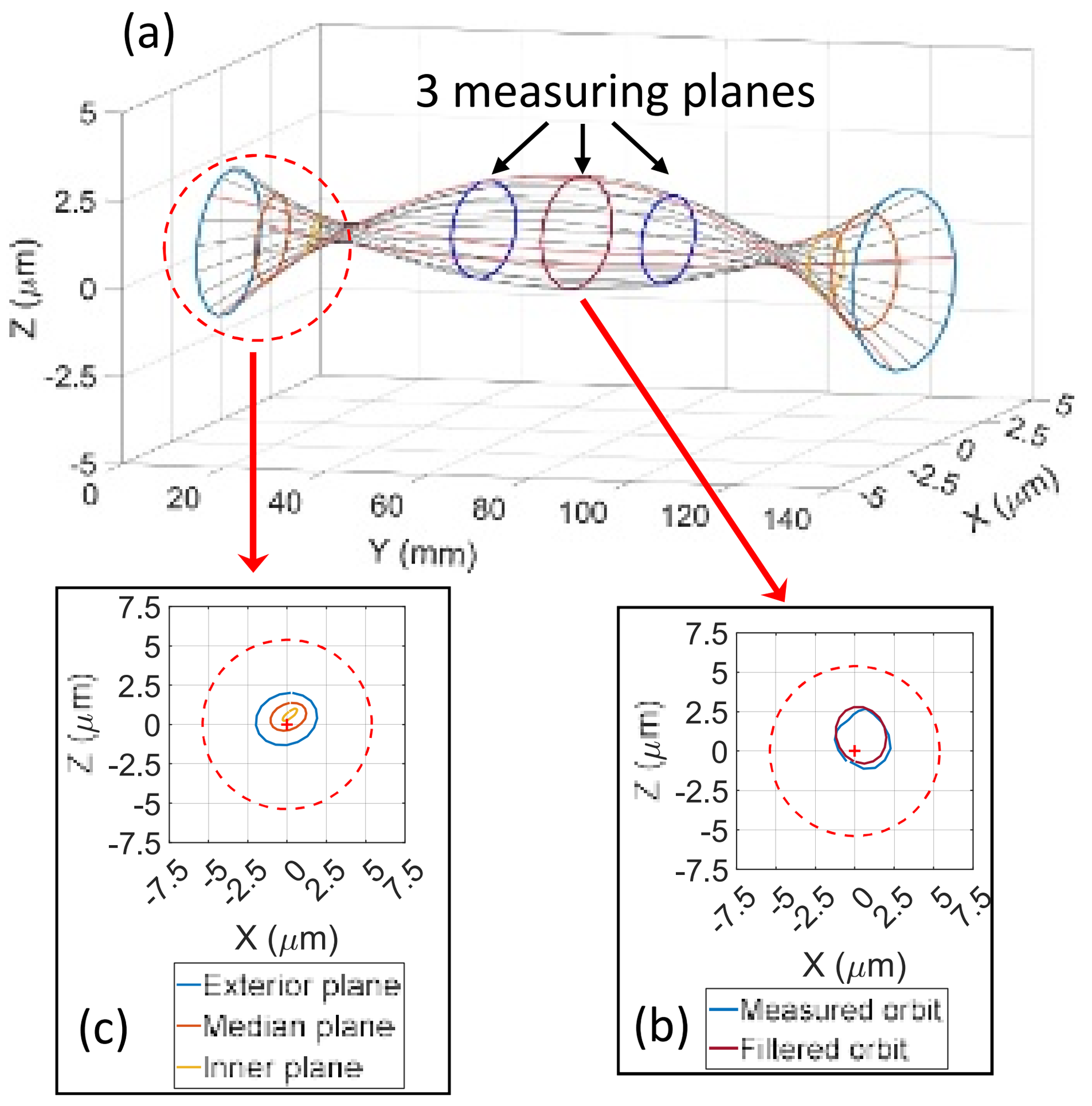
(a)
3 measuring planes
Z (μm)
Y (mm)
X (μm)
(b)
Measured orbit
Filtered orbit
(c)
Exterior plane
Median plane
Inner plane

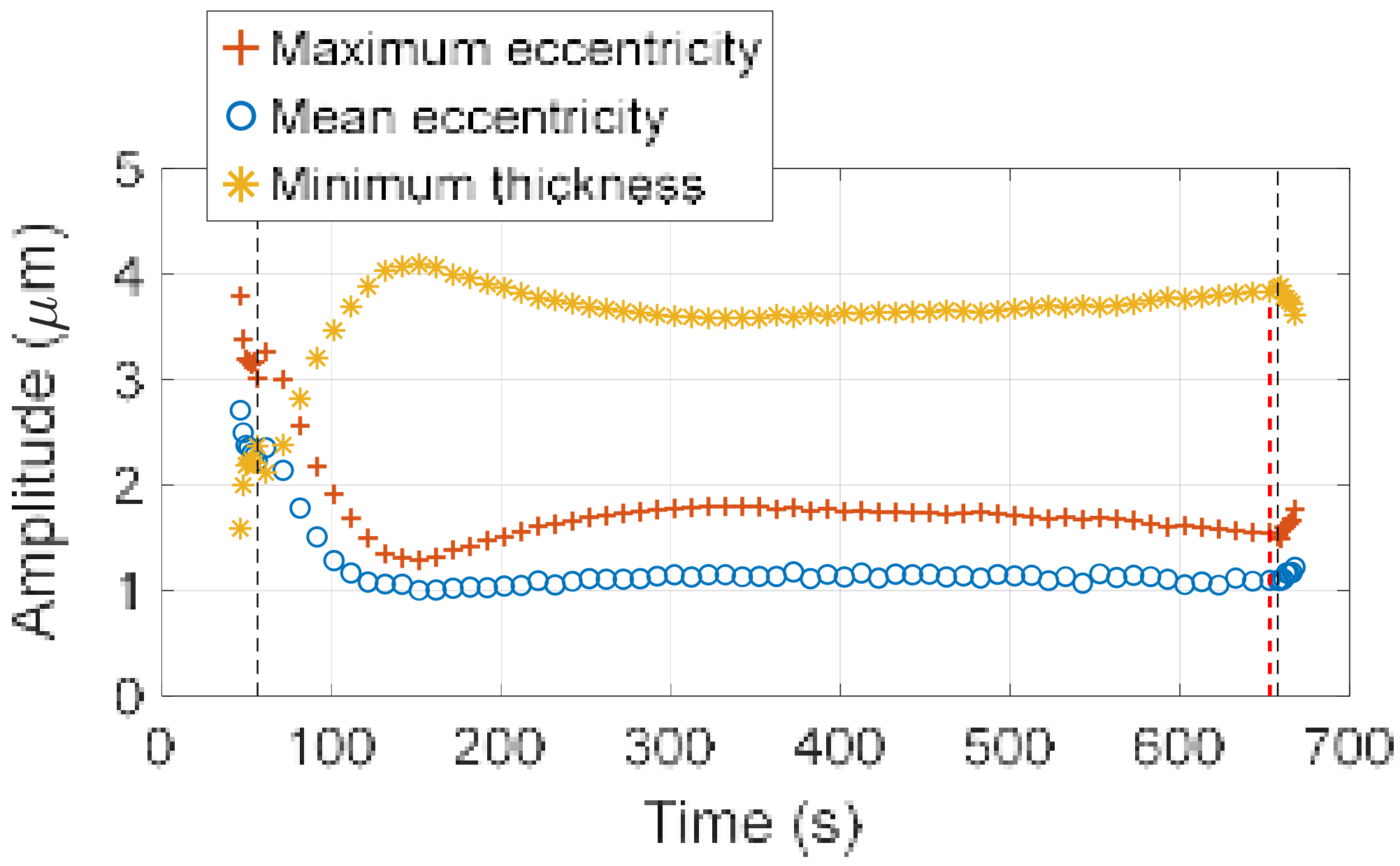
Maximum eccentricity
Mean eccentricity
Minimum thickness
Amplitude (μm)
0
1
2
3
4
5
0
100
200
300
400
500
600
700
Time (s)

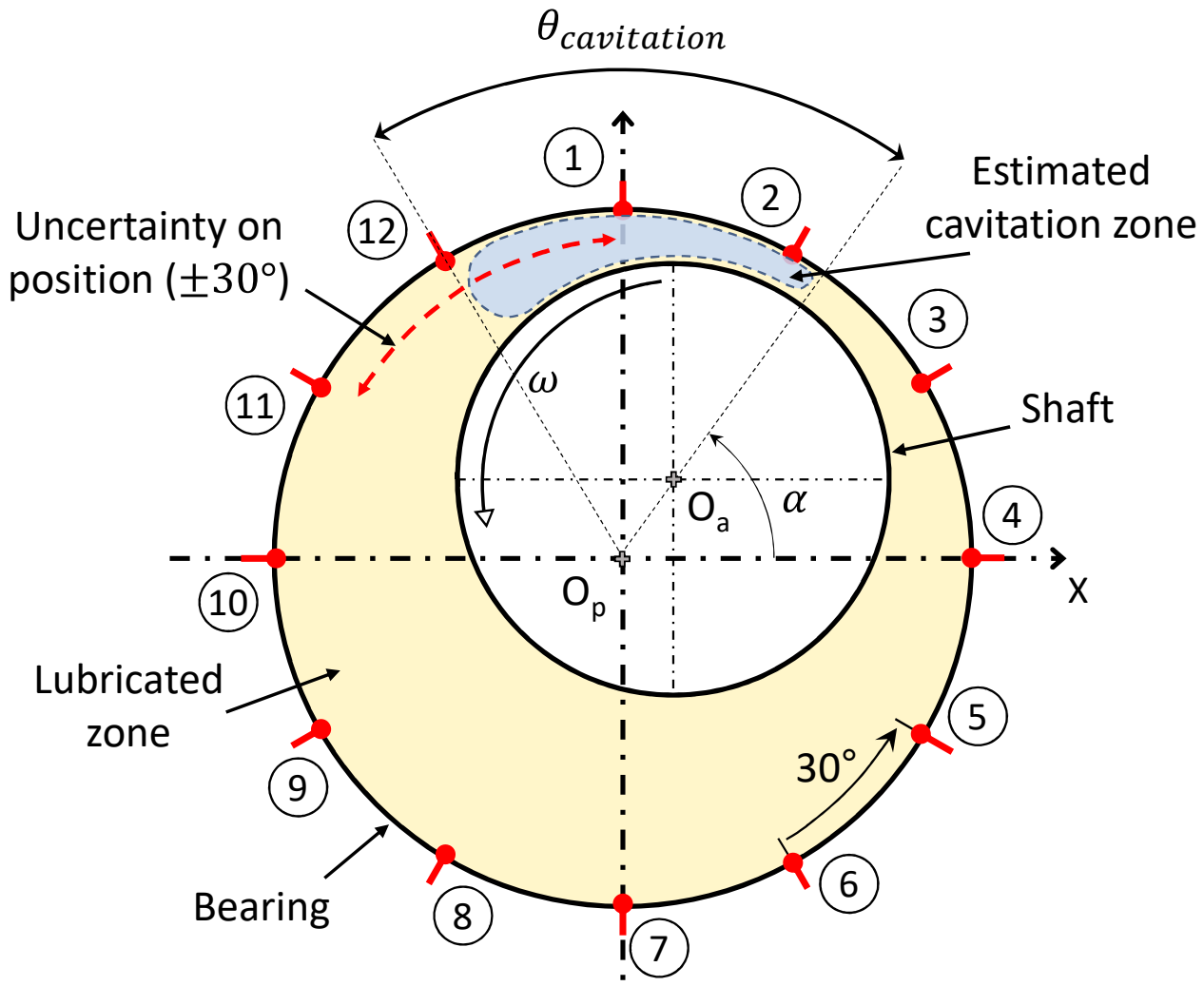
$\theta_{cavitation}$
1
2
3
4
5
6
7
8
9
10
11
12
Estimated cavitation zone
Uncertainty on position ($\pm 30°$)
Shaft
ω
O_a
α
O_p
X
Lubricated zone
30°
Bearing

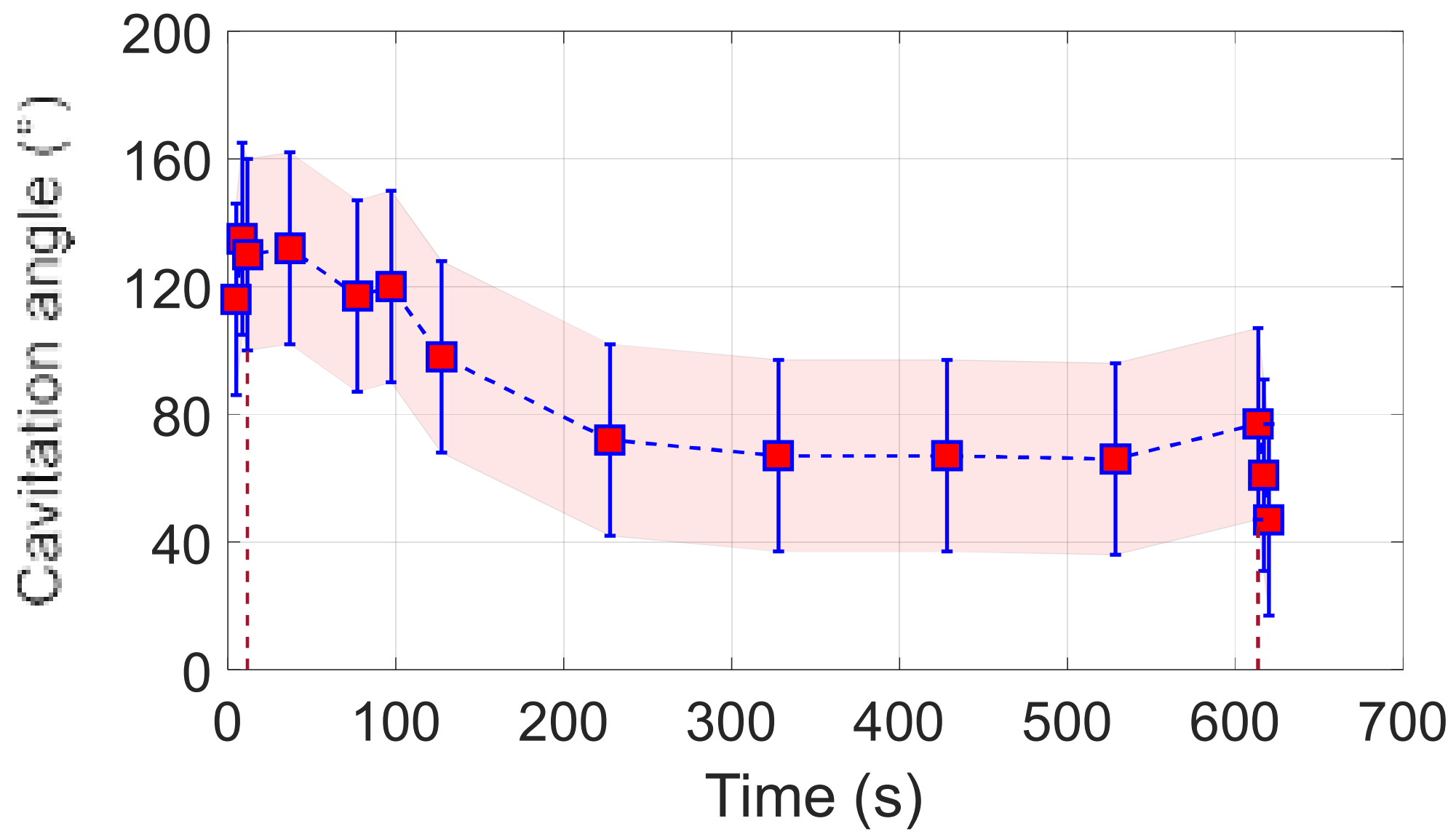
Cavitation angle (°)
200
160
120
80
40
0
0
100
200
300
400
500
600
700
Time (s)

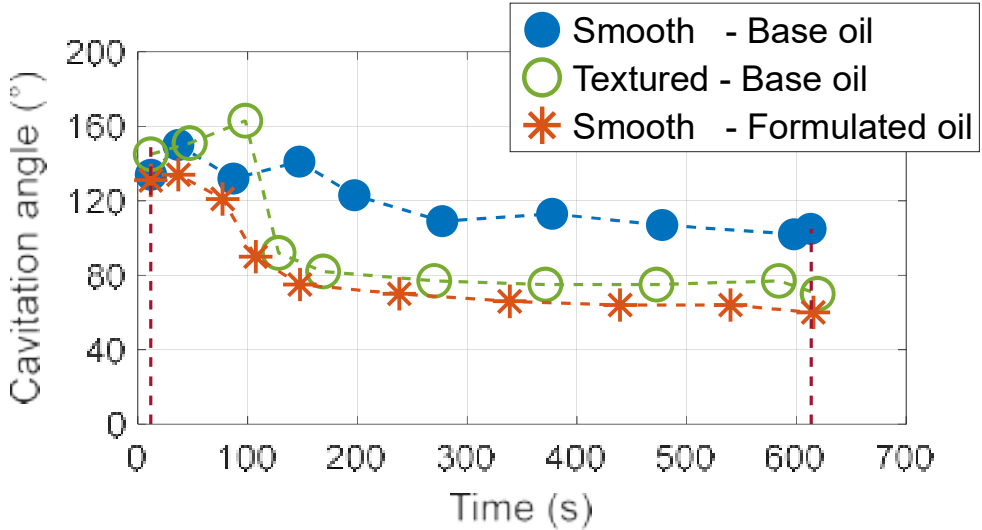
Smooth - Base oil
Textured - Base oil
Smooth - Formulated oil
Cavitation angle (°)
Time (s)
0
40
80
120
160
200
0
100
200
300
400
500
600
700